

Science Department, University of Amsterdam

# AstroParticle Physics

Lecture notes for the 2011 course

# 1 TABLE OF CONTENTS

2	INTRODUCTION .....	3
3	SOFT PHYSICS .....	5
3.1	Scattering.....	5
3.1.1	Green Function .....	6
3.1.2	Perturbation .....	7
3.2	Amplitudes as Partial Waves.....	8
3.3	Elastic and Inelastic Scattering .....	9
3.3.1	Profile functions .....	10
3.4	Regge Phenomenology.....	12
3.5	Total Cross Sections.....	13
3.6	Longitudinal phase space .....	17
4	COSMIC RAYS .....	20
4.1	The spectrum .....	20
4.2	Chemical composition.....	22
4.3	Propagation.....	25
4.4	Galactic source .....	31
4.5	Acceleration .....	32
4.6	Higher Energy .....	37
4.7	Extended Air Showers.....	38
5	Nucleosynthesis .....	44
5.1	Proton to Neutron ratio.....	46
5.2	Deuterium production .....	47
6	Neutrino Oscillations .....	49
6.1	Homestake, SAGE and Gallex.....	50
6.2	Water detectors.....	50
6.3	Water detectors: IMB and Kamiokande.....	51
6.4	Oscillations.....	53
6.5	The SNO experiment.....	54
6.6	Atmospheric Neutrinos .....	56
6.7	The Wolfenstein-Mikheev-Smirnow effect .....	56

## 2 INTRODUCTION

Astroparticle Physics has developed over the years from being the only particle physics available at the beginning of the 20<sup>th</sup> century. At that time the cosmic rays were used as particle beams. With the advent of particle accelerators the particle physics experiments got a controlled environment in which to investigate the interactions of particles and astroparticle physics moved in the direction of investigating the characteristics of the “cosmic beams” rather than their interactions. Of course interactions of the very highest available energies were still investigated in cosmic ray experiments. It is interesting that the maximum available energy has always remained in favour of the cosmic ray experiments even to this day. The maximum available centre of mass energy in cosmic ray interactions is of the order

$$E_{CM} = \sqrt{2E_{CR}m_p} \approx \sqrt{2 \times 10^{11}}[\text{GeV}] \approx 450[\text{TeV}]$$

still about a factor of 30 larger than that obtained by the LHC. Of course the usability of this CM energy is somewhat limited by the fact that less than one of these particles arrive per year on one square kilometre of earth.

In the mean time many other fields of research have been added to the collective field of astroparticle physics.

- Cosmic Ray physics
- Experimental measurements of the parameters of cosmology.
- Cosmic Microwave background
- Dark Matter Searches
- Investigation of the high energy processes in the universe such as Active Galactic Nuclei and Gamma Ray Bursts
- TeV gamma-ray physics
- Neutrino Astrophysics
- Neutrino-less double-beta decay
- .....

By definition then the subjects of the lectures presented here will be somewhat fractured.

We will start with a general discussion on hadronic interactions, which is a basis for understanding cosmic rays. This is necessary not only to understand the properties of the cosmic rays through their interaction in the atmosphere, but also to understand how they propagate through space from where they acquire their energy to Earth.

Next we will discuss what we know about charged cosmic rays: what kind of particles are they, where do they come from and how do they become so energetic. Then we will turn our attention on the evolution of the universe from the Big Bang to now and will investigate the generation of baryons and nuclei. Here we will find the first indication of the necessity of the three quark families of the standard model. We will from the present abundance of helium be able to limit the number of light neutrino flavours.

To take a step further in the understanding of the evolution of our universe we will investigate the cosmic microwave background (CMB). Specifically the fluctuations in the

temperature of the CMB will show that the universe as we know it is only a small fraction of the matter in the cosmos. This will bring us to the question of Dark Matter. We will review the evidence for dark matter, touching on the way on subjects like gravitational (micro)-lensing, dark matter detection techniques and possible candidates for dark matter.

Finally we will turn our attention back to the cosmic rays, but now not charged but neutral: In other words the high energy photons and neutrinos.

### 3 SOFT PHYSICS

Generally the word soft physics is reserved for describing our lack of knowledge about the major fraction of the total hadronic cross section. In other words the Standard Model of particle physics describes hard processes, mostly  $2 \rightarrow 2$  processes or production of massive objects like Ws, Zs, Hs or top-quarks. To understand most of what goes on in the universe today this has very little relevance.

For instance, understanding the propagation of particles through the cosmos depends completely on total cross sections rather than on the hard processes described by the Standard Model. The soft physics was all one had in the beginning of particle physics and in the 1950s and 1960s many systematic studies were made of these processes. Many general descriptions were made in a sort of phenomenological way. Mathematical requirements of continuity, extendibility and crossing symmetry led to general behaviours of total cross sections to be derived and the few parameters necessary to give a description of the data were extracted from experiment. In this way all soft physics is described very concisely.

#### 3.1 Scattering

An easy way to look at scattering of a particle with mass  $m$  off a second particle is in the wave approximation, using the Schrödinger equation

$$(\nabla^2 + k^2)\psi(\vec{r}) = 2mV(\vec{r})\psi(\vec{r}) \quad (3-1)$$

Where the second particle is described by a potential. We off course take  $\hbar = c = 1$ , from which follows  $k^2 = 2mE$ . What we have to describe is the scattering of a particle entering effectively from  $z = -\infty$ , feeling the effect of the scattering potential very close to the target and scattering with some probability to  $(\vec{r}, |\vec{r}| = \infty)$ . At  $z = -\infty$  the effect of the potential is negligible so we can approximate the solution by the solution of (3-1) with  $V=0$ . This is off course a plane wave given by:

$$\varphi_{in}(\vec{r}) = e^{i\vec{k}_{in}\cdot\vec{r}} \quad (3-2)$$

We can now define the flux of the incoming particle by the current density

$$\vec{J}_{in} = \frac{1}{2mi}(\varphi_{in}^*\nabla\varphi_{in} - \varphi_{in}\nabla\varphi_{in}^*) = \frac{\vec{k}_{in}}{m} = \vec{\beta}_{in} \quad (3-3)$$

The particle is scattered at the target and so the solution to the scattering problem will be a superposition of the incoming plane wave and a number of spherical waves that have their origin in a scattering centre somewhere in the region where the potential differs significantly from zero. We will solve the equation by introducing a Green function that has the property:

$$(\nabla^2 + k^2)G(\vec{r}|\vec{r}') = \delta(\vec{r} - \vec{r}') \quad (3-4)$$

It is then clear that we can write the solution of (3-1) as

$$\Phi(\vec{r}) = \varphi_{in}(\vec{r}) + 2m \int G(\vec{r}|\vec{r}') V(\vec{r}') \Phi(\vec{r}') d\vec{r}' \quad (3-5)$$

We now need to derive the Green function before we can proceed with the solution of the problem.

### 3.1.1 Green Function

The Green function is the solution to the equation

$$(\nabla^2 + k^2)G(\vec{r}|\vec{r}') = \delta(\vec{r} - \vec{r}') \quad (3-6)$$

which is solvable using the integral expression for the delta function:

$$\delta(\vec{r} - \vec{r}') = \frac{1}{(2\pi)^3} \int e^{i\vec{q}\cdot(\vec{r}-\vec{r}')} d^3q \quad (3-7)$$

From which follows

$$G(\vec{r}|\vec{r}') = G(\vec{r} - \vec{r}') = (\nabla^2 + k^2)^{-1} \frac{1}{(2\pi)^3} \int e^{i\vec{q}\cdot(\vec{r}-\vec{r}')} d^3q = \frac{1}{(2\pi)^3} \int \frac{e^{i\vec{q}\cdot(\vec{r}-\vec{r}')}}{(k^2 - q^2)} d^3q \quad (3-8)$$

which after integration over the angles, with  $x = |\vec{r} - \vec{r}'|$ , is

$$G(x) = \frac{1}{4\pi^2 ix} \int_{-\infty}^{\infty} \frac{q e^{iqx}}{(k^2 - q^2)} dq \quad (3-9)$$

This function has poles in  $q=+k$  and  $q=-k$  so by choosing one of the two independent non-trivial integration paths given in Figure 3-1

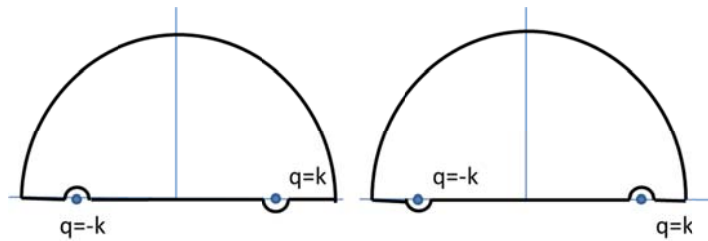


Figure 3-1: Integration contours for calculating the Green Function.

Using the using Cauchy's theorem that the integral round a pole is equal to  $2\pi i$  times the Residue of the function at the pole, the following solutions are obtained.

$$G_+(x) = -\frac{e^{ikx}}{4\pi x} \quad \text{and} \quad G_-(x) = -\frac{e^{-ikx}}{4\pi x} \quad (3-10)$$

Clearly the + solution gives an indication of an outgoing wave and the – solution an incoming wave.

Therefore using the  $G_+(x)$  for our problem we find that the general solution (3-1) is

$$\Phi(\vec{r}) = \varphi_{in}(\vec{r}) + \frac{m}{2\pi} \int \frac{e^{-ik|\vec{r}-\vec{r}'|}}{|\vec{r}-\vec{r}'|} V(\vec{r}') \Phi(\vec{r}') d\vec{r}' \quad (3-11)$$

As we are only interested in the solution for large values of  $r$  we can rewrite  $k|\vec{r}-\vec{r}'| \approx kr - (\vec{k}_{out} \cdot \vec{r}')$  where we have introduced  $\vec{k}_{out} = k \frac{\vec{r}}{|\vec{r}|}$ . It then follows that the solution to our problem is given by

$$\Phi(\vec{r}) = \varphi_{in}(\vec{r}) + f(\vec{k}_{in}, \vec{k}_{out}) \frac{e^{ikr}}{r} \quad (3-12)$$

With

$$f(\vec{k}_{in}, \vec{k}_{out}) = -\frac{m}{2\pi} \int e^{-i\vec{k}_{out} \cdot \vec{r}'} V(\vec{r}') \Phi(\vec{r}') d\vec{r}' \quad (3-13)$$

Of course the problem of the calculation of the scattering amplitude  $f$  still has the total wavefunction solution behind the integral sign so we haven't really solved things yet. This can always be done using a perturbation expansion. For the time being we are just interested in some general characteristics of the solution. Let's calculate the outward going current density. Of course we will only be interested in the radial component which is given by:

$$j_r = \frac{1}{2mi} \left( \varphi_{sc}^* \frac{\partial}{\partial r} \varphi_{sc} - \varphi_{sc} \frac{\partial}{\partial r} \varphi_{sc}^* \right) = \frac{k}{mr^2} f f^* = \frac{k}{mr^2} |f|^2 \quad (3-14)$$

So the flux into an opening angle  $d\Omega$  is  $r^2 d\Omega j_r$  from which it follows that

$$\frac{d\sigma}{d\Omega} = \frac{j_r r^2}{|j_{in}|} = |f(\vec{k}_{in}, \vec{k}_{out})|^2 \quad (3-15)$$

### 3.1.2 Perturbation

To calculate the scattering we make an approximation that the potential gives only a small perturbation to the incoming wave and so we can use  $\varphi_{in}(\vec{r}')$  rather than  $\Phi(\vec{r}')$  in (3-13). Which after a little bit of algebra leads to

$$f(\vec{q}) = -\frac{m}{2\pi} \int e^{i\vec{q} \cdot \vec{r}} V(\vec{r}) d^3r \quad (3-16)$$

### 3.2 Amplitudes as Partial Waves

In this chapter we will take a look at a general description of scattering in terms of partial waves. We can do this because of the spherical symmetry of the scattering problem. We can then describe the scattering on a potential by the sum of an incoming plane wave and an outgoing spherical wave. In fact we can write the incoming plane wave as a sum over the partial waves where each partial wave corresponds to a wave of definite angular momentum.

$$\varphi_{in} = \sum_{l=0}^{\infty} (2l+1) i^l j_l(kr) P_l(\cos \vartheta) \quad (3-17)$$

Where the functions  $j_l(kr)$  are spherical Bessel functions describing the radial distribution and  $P_l(\cos \vartheta)$  are the Legendre polynomials describing the angular distribution of the partial wave. For large values of  $kr$  the Bessel functions behave as:

$$j_l(kr) \approx \frac{\sin\left(kr - \frac{l\pi}{2}\right)}{kr} \quad (3-18)$$

So asymptotically we can write the incoming wave as

$$\varphi_{in}(r, \vartheta) = \frac{1}{kr} \sum_{l=0}^{\infty} (2l+1) i^l P_l(\cos \vartheta) \rho_l(kr) \quad (3-19)$$

Where  $\rho_l$  is given by

$$\rho_l(kr) = \sin\left(kr - \frac{l\pi}{2}\right) = \frac{i}{2} \left[ e^{-i\left(kr - \frac{l\pi}{2}\right)} - e^{i\left(kr - \frac{l\pi}{2}\right)} \right] \quad (3-20)$$

Of course we can do the same decomposition for the solutions of the Schrödinger equation

$$\Phi(r, \vartheta) = \frac{1}{kr} \sum_{l=0}^{\infty} (2l+1) i^l P_l(\cos \vartheta) R_l(kr) \quad (3-21)$$

Where we have introduced some unknown functions which have to be solutions of the

$$\left[ \frac{d^2}{dr^2} - \frac{l(l+1)}{r^2} + k^2 \right] R_l(kr) = \frac{2m}{\hbar^2} V(r) R_l(kr) \quad (3-22)$$

Schrödinger equation written for convenience in spherical coordinates

If we now look at the scattering problem again the full solution should contain the incoming plane wave and an outgoing spherical wave. It is then reasonable to derive the  $R$  functions from the  $\rho$  functions whereby the outgoing spherical waves present in the decomposition of the incoming plane wave get modified by the scattering

$$R_l(kr) = \frac{i}{2} \left[ e^{-i\left(kr - \frac{l\pi}{2}\right)} - S_l e^{i\left(kr - \frac{l\pi}{2}\right)} \right] \quad (3-23)$$

If we now again write the solution of the problem as

$$\Phi(r, \vartheta) = \varphi_i(r, \vartheta) + \varphi_{sc}(r, \vartheta) = \varphi_i(r, \vartheta) + f(\vartheta) \frac{e^{ikr}}{r} \quad (3-24)$$

Then using (3-23) the scattering amplitudes are given by

$$f(\vartheta) = \frac{i}{2k} \sum_{l=0}^{\infty} (2l+1)(1-S_l)P_l(\cos \vartheta) \quad (3-25)$$

Furthermore we know that to conserve the total normalisation of the waves that we have to require  $|S_l| = 1$  and so we can write

$$\begin{aligned} S_l &= e^{2i\delta_l} \\ (1-S_l) &= -2i \sin \delta_l e^{i\delta_l} \\ &= -2i \sin \delta_l (\cos \delta_l + i \sin \delta_l) \end{aligned} \quad (3-26)$$

The scattering amplitude is then given in terms of the phaseshift  $\delta_l$  by

$$f(\vartheta) = \frac{1}{k} \sum_{l=0}^{\infty} (2l+1) \sin \delta_l e^{i\delta_l} P_l(\cos \vartheta) = \frac{1}{k} \sum_{l=0}^{\infty} (2l+1) f_l P_l(\cos \vartheta) \quad (3-27)$$

And the  $f_l$  are called the partial wave amplitudes.

### 3.3 Elastic and Inelastic Scattering

In the above the normalisation of the wavefunction was taken as  $\beta$ , however using relativistic particles it is more convenient to normalise the wave function to 1, i.e. one particle, so that the current density is given by:

$$\vec{J}_{in} = \frac{1}{2k_{in}i} (\varphi_{in}^* \nabla \varphi_{in} - \varphi_{in} \nabla \varphi_{in}^*) \quad (3-28)$$

And likewise for the radial current density. Introducing the scattering function  $S(\vec{r})$  as a generalisation of the potential and the profile function  $\Gamma(\vec{r}) = 1 - S(\vec{r})$  we can write the outgoing wavefunction as

$$\psi(\vec{r}) = \frac{-ik}{2\pi} \frac{e^{ikr}}{r} \int S(\vec{r}') e^{i\vec{q} \cdot \vec{r}'} d^3r' \quad (3-29)$$

And the elastic scattering amplitude

$$f(\vec{q}) = \frac{ik}{2\pi} \int \Gamma(\vec{r}') e^{i\vec{q} \cdot \vec{r}'} d^3r' \quad (3-30)$$

To make it a little easier we will approximate the scattering target as a disc  $\Gamma(\vec{r}) = \Gamma(\vec{b})\delta(z)$  so that we get

$$f(\vec{q}) = \frac{ik}{2\pi} \int \Gamma(\vec{b}) e^{i\vec{q} \cdot \vec{b}} d^2b \quad (3-31)$$

The differential elastic cross section is given by

$$\frac{d\sigma}{d\Omega} = |f(\vec{q})|^2 \quad (3-32)$$

Integrating this over the full solid angle gives the total elastic cross section

$$\sigma_{el} = \int |f(\vec{q})|^2 \frac{d^2q}{k^2} \quad (3-33)$$

With

$$|f(\vec{q})|^2 = \iint \Gamma(\vec{b}) \Gamma^*(\vec{b}') e^{i\vec{q}\cdot(\vec{b}-\vec{b}')} d^2b d^2b' \quad (3-34)$$

And using

$$\delta(\vec{b} - \vec{b}') = \frac{1}{(2\pi)^2} \int e^{i\vec{q}\cdot(\vec{b}-\vec{b}')} d^2q \quad (3-35)$$

the total elastic cross section is given by

$$\sigma_{el} = \int |\Gamma(\vec{b})|^2 d^2b \quad (3-36)$$

We now turn to calculating the inelastic cross section. This is of course just the incoming flux minus the outgoing elastic flux:

$$\begin{aligned} \sigma_{inel} &= \int d^2b - \int j_r r^2 d\Omega = \int d^2b - \frac{k^2}{4\pi^2} \iiint S(\vec{b}) S^*(\vec{b}') e^{i\vec{q}\cdot(\vec{b}-\vec{b}')} d^2b' d^2b \frac{d^2q}{k^2} \\ &= \int (1 - |S(\vec{b})|^2) d^2b = \int (2\text{Re}\Gamma(\vec{b}) - |\Gamma(\vec{b})|^2) d^2b \end{aligned} \quad (3-37)$$

From which it follows that the total cross section is given by

$$\sigma_{tot} = 2\text{Re} \int \Gamma(\vec{b}) d^2b \quad (3-38)$$

And comparing this to the elastic scattering amplitude at zero momentum transfer we come to the optical theorem which states that

$$\sigma_{tot} = \frac{4\pi}{k} \text{Im}f(0) \quad (3-39)$$

### 3.3.1 Profile functions

#### *Uniform disc*

A uniform density disc is given as

$$\begin{aligned}\Gamma(b) &= a \quad \text{for } 0 < b < R \\ \Gamma(b) &= 0 \quad \text{for } b > R\end{aligned}\tag{3-40}$$

from which it follows that

$$f(q) = \frac{ik}{2\pi} \int \Gamma(\vec{b}) e^{i\vec{q}\cdot\vec{b}} d^2b = ika \int_0^R J_0(qb) b db\tag{3-41}$$

from which we can derive, using

$$\int_0^A Z J_0(Z) dZ = A^2 J_1(A)\tag{3-42}$$

that

$$f(q) = ikaR^2 \frac{J_1(qR)}{qR}\tag{3-43}$$

and because

$$\frac{J_1(x)}{x} \xrightarrow{x \rightarrow 0} \frac{1}{2} e^{-\frac{x^2}{8}}\tag{3-44}$$

the total cross section becomes

$$\sigma_{tot} = \frac{4\pi}{k} \frac{1}{2} kaR^2 = 2\pi R^2\tag{3-45}$$

The differential elastic cross section is

$$\frac{d\sigma}{d\Omega} |_{el} = a^2 k^2 R^4 \left( \frac{J_1(qR)}{qR} \right)^2 \rightarrow \frac{d\sigma}{dq^2} |_{el} = \frac{d\sigma}{dt} |_{el} = \pi a^2 R^4 \left( \frac{J_1(qR)}{qR} \right)^2\tag{3-46}$$

which for small t becomes

$$\left. \frac{d\sigma}{dt} \right|_{el} = \pi a^2 R^4 e^{-\frac{q^2 R^2}{4}} = \pi a^2 R^4 e^{\frac{R^2}{4} t}\tag{3-47}$$

so the slope of the elastic cross section in t gives an indication of the size of the disc. In this case the total cross section is twice the area of the disc and the elastic cross section is given by the area of the disc.

### *Gaussian profile*

With the profile function given by  $\Gamma(b) = \Gamma(0) e^{-\left(\frac{b}{b_0}\right)^2}$  it is easy to derive that

$$\begin{aligned}
\sigma_{tot} &= 2\pi\Gamma(0)b_0^2 \\
\sigma_{el} &= \frac{1}{2}\pi\Gamma(0)^2b_0^2 \\
\frac{d\sigma}{dt} &= \frac{\pi}{4}\Gamma(0)^2b_0^2e^{\frac{b_0^2}{2}t}
\end{aligned}
\tag{3-48}$$

Both profile functions predict an exponential shape of the elastic  $t$  distribution at small  $t$  the uniform disc shows a characteristic diffraction pattern with a zero point given by the square first order Bessel function. Experimentally the ratio of total to elastic cross section favours the Gaussian profile. The differential cross section shows an exponential behaviour at small  $t$ , but at large  $t$  a diffractive minimum is observed (see ),

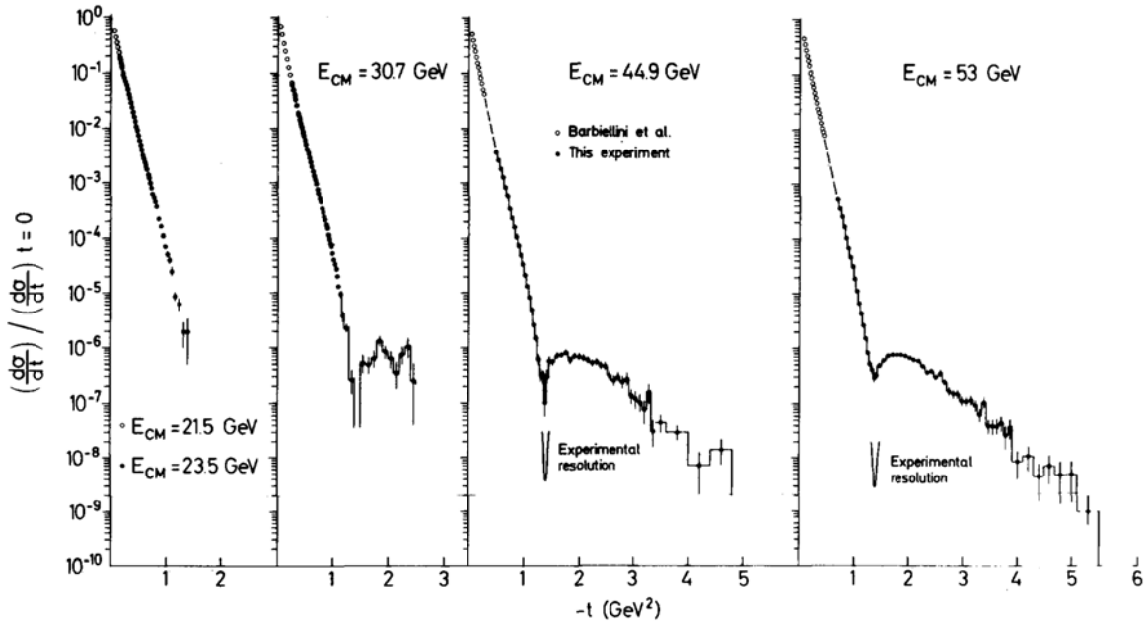


Figure 3-2: Elastic proton proton scattering showing the diffractive minimum

making the geometrical picture of the proton a little more complicated. Of course here we have just used the wave equation to extract some of the characteristics of scattering cross sections so in principle the profile function has to be seen as a convolution of the profiles of the beam and target.

### 3.4 Regge Phenomenology

To get a handle on the behaviour of the total cross section as a function of the centre of mass energy we will now turn to Regge-Müller analysis. This analysis started from an observation that when one plots the angular momentum of particles such as  $r$  versus their mass squared then the particles with the same  $G$ -parity fall on a straight line. So if one for instance in  $p\bar{p}$  collisions creates these resonances at a particular  $s$  value their behaviour is very similar. If one now extends the investigation to the  $t$ -channel exchange of one of these particles in  $pp$  collisions one expects that it will somehow reflect the equality of these particles and they will behave similarly. To do this we first introduce the invariant amplitude

rather than the one we have been working with so far. The invariant cross section is in this case given as

$$\sigma_{inv} = \frac{s}{\pi} \frac{d\sigma}{dt} = \frac{1}{16\pi^2 s} |F(s, t)|^2 \quad (3-49)$$

And in terms of the invariant amplitude the optical theorem takes on the form

$$\sigma_{tot}(s) = \frac{1}{s} \text{Im } F(s, 0) \quad (3-50)$$

### 3.5 Total Cross Sections

The invariant amplitude can of course like any function be described as infinite sum of partial waves

$$F(s, t) = \frac{8\pi\sqrt{s}}{k} \sum_{l=0}^{\infty} (2l+1) f_l(s) P_l(\cos \vartheta) \quad (3-51)$$

This can be converted via a Sommerfeld-Watson transformation to an integral over  $l$ , which is now a complex variable. One must of course assume that the partial wave amplitudes are continuous and extendible into the complex plane.

$$F(s, t) = \frac{8\pi\sqrt{s}}{k} \frac{1}{2\pi i} \int \frac{\pi(2l+1) f(s, l) P_l(\cos \vartheta) dl}{\sin \pi l} \quad (3-52)$$

The expectation is then that in the complex plane there are poles which correspond to the trajectories of equally behaving particles.

$$F(s, t) = \frac{8\pi\sqrt{s}}{k} \sum_i \frac{\pi(2\alpha_i + 1) R_{\alpha_i}(s) P_{\alpha_i}(\cos \vartheta)}{\sin \pi \alpha_i} \quad (3-53)$$

Where  $R_{\alpha_i}(s)$  is the residue of the partial wave amplitude in the pole occurring at  $\alpha_i$ . So we have taken an infinite sum of partial waves and have transformed it into hopefully a finite sum over poles. So we can now specify the process we are interested in.

$$p_1 + p_2 \rightarrow p_3 + p_4 \quad (3-54)$$

To see the effect of the Regge poles we first look at the crossed channel

$$p_1 + \bar{p}_3 \rightarrow \bar{p}_2 + p_4 \quad (3-55)$$

Where we expect the resonances to occur that in the first reaction are exchanged particles. It is clear that for this reaction the partial wave expansion is valid and we can then lumping everything except the Legendre polynomial together it looks like:

$$F(\bar{s}, \bar{t}) = \sum_i \beta_i(\bar{s}) P_{\alpha_i}(\cos \bar{\vartheta}) \quad (3-56)$$

Where we have indicated by the bar over the variables that we are dealing with the crossed channel to the one we really want. We now invoke the crossing symmetry that states that the invariant amplitude in the crossed channel is equal to that of the non-crossed channel as long as we replace  $\bar{s}$  with  $t$  and  $\bar{t}$  with  $s$ . In other words:

$$F(\bar{s}, \bar{t}) = F(t = \bar{s}, s = \bar{t}) \quad (3-57)$$

For the crossed channel we have  $\bar{t} = (\mathbf{p}_1 - \bar{\mathbf{p}}_2)^2$  which gives

$$\bar{t} = 2m^2 - 2E_1\bar{E}_2 - 2p_1\bar{p}_2 \cos \bar{\vartheta} = 2m^2 - 2E^2 + 2(E^2 - m^2) \quad (3-58)$$

where for the last equality we have used the fact that we work in the centre of mass frame (invariant amplitude) and that we are dealing with elastic scattering. From this it follows that

$$\cos \bar{\vartheta} = \frac{\bar{s} + 2\bar{t} - 4m^2}{\bar{s} \left(1 - \frac{4m^2}{\bar{s}}\right)} \quad (3-59)$$

Changing to the non-crossed channel we have then

$$\cos \vartheta = \frac{t + 2s - 4m^2}{t \left(1 - \frac{4m^2}{t}\right)} \approx \frac{s}{4m^2} \quad (3-60)$$

This is for almost all situations a large number so we can take the behaviour of the Legendre polynomials  $P_\alpha(x) \xrightarrow{x \rightarrow \infty} x^\alpha$  so we find that the asymptotic behaviour of the amplitude is

$$F(s, t) = \sum_i \beta_i(t) \left(\frac{s}{s_0}\right)^{\alpha_i(t)} \quad (3-61)$$

And so using the optical theorem we get to the total cross section:

$$\sigma_{tot} = \frac{1}{s} \sum_i \beta_i(0) \left(\frac{s}{s_0}\right)^{\alpha_i(0)} = \sum_i \beta_i(0) \left(\frac{s}{s_0}\right)^{\alpha_i(0)-1} \quad (3-62)$$

So let's now see what these values of  $\alpha_i$  are. In Figure 3-3 the trajectory of the  $\rho$  is shown. The right hand side of the plot where  $M^2$  is positive the resonances occur at equal intervals as the angular momentum increases. These coincide with the  $p\bar{p} \rightarrow (\rho; \omega; A_2; f) \rightarrow p\bar{p}$  whereas

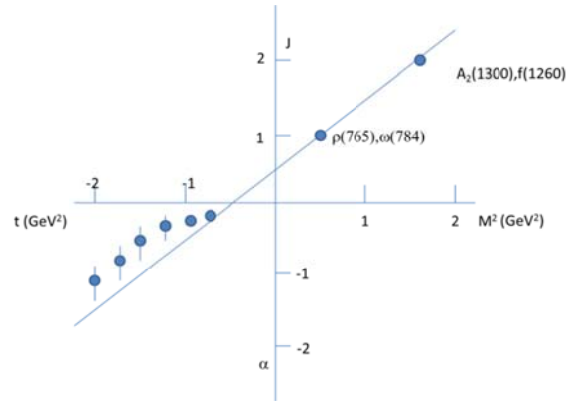


Figure 3-3: the  $\rho$  trajectory the slope of the trajectory is measured to be 0.95 and the intercept is at 0.5. The measurements in the virtual range come from a Regge fit to data of  $pp \rightarrow pX$  where the  $x$  value of the final state proton lies in the region  $0.5 < x < 0.8$ . The slope of the trajectory in the virtual range is 0.75, with an intercept that is compatible with 0.5.

the righthand side of the plot coincides with negative mass squared and so to the virtual exchange of  $(\rho; \omega; A_2; f)$ . The value of  $\alpha(0)$  is the value of the angular momentum at the intercept. In the case of the  $(\rho; \omega; A_2; f)$  trajectory  $\alpha(0) \approx 0.5$ . We then predict that the total cross section in  $pp$  collisions will decrease as  $\left(\frac{s}{s_0}\right)^{-0.5}$  if the exchange is dominated by the exchange of  $(\rho; \omega; A_2; f)$  this is indeed what is seen at low values of  $s$ . The other well-known trajectory is that of the  $\pi$  that has its intercept at 0 and therefore predicts a  $\left(\frac{s}{s_0}\right)^{-1}$  behaviour.

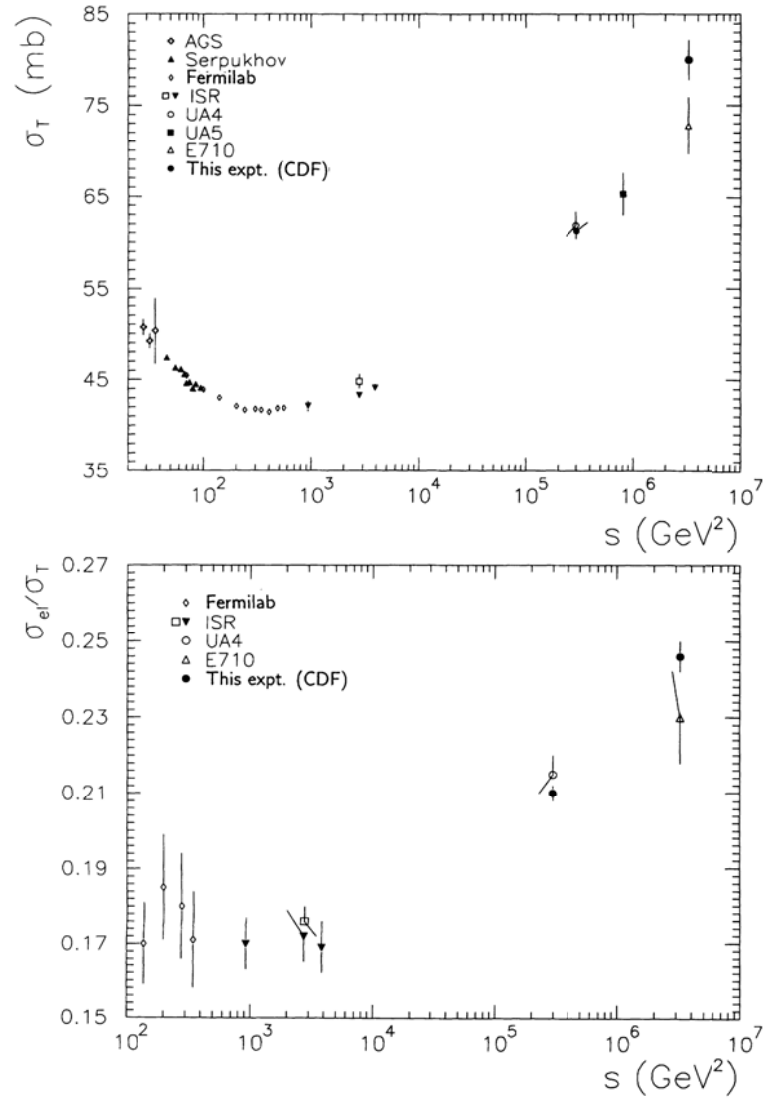


Figure 3-4: Total cross section versus centre of mass energy squared,  $s$  (top) and the elastic fraction (bottom)

In the early 70s the total pp cross section seemed to be flattening off and most theoreticians were convinced the cross section would become constant. This would mean that there should be a trajectory that had an intercept at 1. This did not exist. It was therefore invented by Pommeranchuk and has thereafter been known as the Pomeron (or the P-word). As we all know the cross section did not remain constant but started to rise. So the Pomeron received an intercept greater than 1. The present preferred value is 1.08. These days the Pomeron is seen as a colourless exchange of a sort of gluonic particle. In fact there have been measurements performed at HERA that claim to have measured the structure function of the Pomeron and see that it is dominated by gluon structure. Be that as it may the fact that we parameterize the cross section as a power of the centre of mass energy where the power is larger than 1 is somewhat perverse. This cannot continue this way as this would finally violate unitarity. These days the rise in the total cross section is ascribed to the very large increase in the gluon density at low values of the Bjorken  $x$ . In fact the shape of the function describing the gluon distribution in the PDF fits to the structure functions has been taken directly from the value of

the Pomeron intercept. In the case of the cross section being driven by the increase in the gluon density we have at least the possibility of introducing a stop to this growth through the process of recombination.

When dealing with extrapolations of cross sections beyond our present experimental knowledge it is certainly necessary to proceed with caution.

### 3.6 Longitudinal phase space

The general interaction of a proton with another proton is a superficial glance where the gluons in the one proton interact with the gluons in the other. This leads most likely to colour exchange (although sometimes the exchanged gluons compensate and we have elastic scattering, and we call the exchange a Pomeron) and so we are left in the final state with a colour field stretching from the one “proton” to the other “proton”. Because of the characteristics of QCD this colour field has little transverse extension. This leads to an increase in the field energy density as the colour charges move away from one another. The energy density increases so much that finally there is locally enough energy to produce a quark anti-quark pair and some of the centre of mass energy will be transformed into mass. This pair will typically be travelling in one or the other direction and we therefore have two strings each with a smaller centre of mass energy, but still both with an increasing string tension. This will proceed until the quarks and anti-quarks of opposite colour form bound state mesons and take not only mass but also kinetic energy out of the colour field. This mechanism has been simulated with the Jetset MonteCarlo. The simulation is well capable of describing the hadronisation that takes place in interactions, at the cost of course of many parameters. Because of the almost one dimensional character of the colour field the simulation assumes that the colour charges are connected via a string which has an energy density or string constant (equivalent to the spring constant in an oscillator) of 1GeV/fm.

When one starts to look at the details of hadronisation one finds that not only pions are formed but also kaons. These can of course be easily accommodated by the fact that a strange quark anti-quark pair gets created from the energy in the field. Experimentally one finds, that the number of kaons produced is about one third of the number of pions. The argument given for this is that the strange quark has more mass and so the string must stretch further to produce a strange pair whereas it should not in the meantime produce an up or down quark pair. In the end this is parameterized by giving the strange quark a production probability of 0.33. It is of course also possible to produce coloured objects with 2 quarks, so in the string di-quark di-anti-quarks can be formed which behave similarly to quark anti-quarks because only their colour is important. This allows for baryon production inside the colour field. This is parameterized with the di-quark probability, which is set such that the roughly 8% of baryons produced in the fragmentation are reproduced.

In this model there is essentially no transverse momentum, however in typical minimum bias events the transverse momentum behaves roughly as  $\frac{d\sigma}{dp_T^2} = e^{-ap_T^2}$  where  $a$  is of the order 6 which means that the typical transverse momentum of a particle is around 300 MeV. In the model, which is quite well substantiated by data, the transverse momentum is randomly chosen and then locally compensated.

The JETSET model is quite successful at describing the data. It leads to a distribution of particles that is approximately flat in rapidity:

$$y = \frac{1}{2} \ln \frac{E + p_L}{E - p_L} \quad (3-63)$$

The incoming protons have a rapidity of  $y = \ln \frac{\sqrt{s}}{m_p}$  which is the limit of the rapidity of other particles produced in the interaction. As an example At the ISR at  $\sqrt{s} = 60$  GeV the particle production spread between  $-4 < y < 4$  at the Tevatron it covers  $-7.5 < y < 7.5$  and at the full energy in LHC it will range from  $-9.5 < y < 9.5$ .

**Show that when transforming from one Lorentz frame to another along the collision axis, that  $y$  transforms into  $y + \text{a constant}$ .**

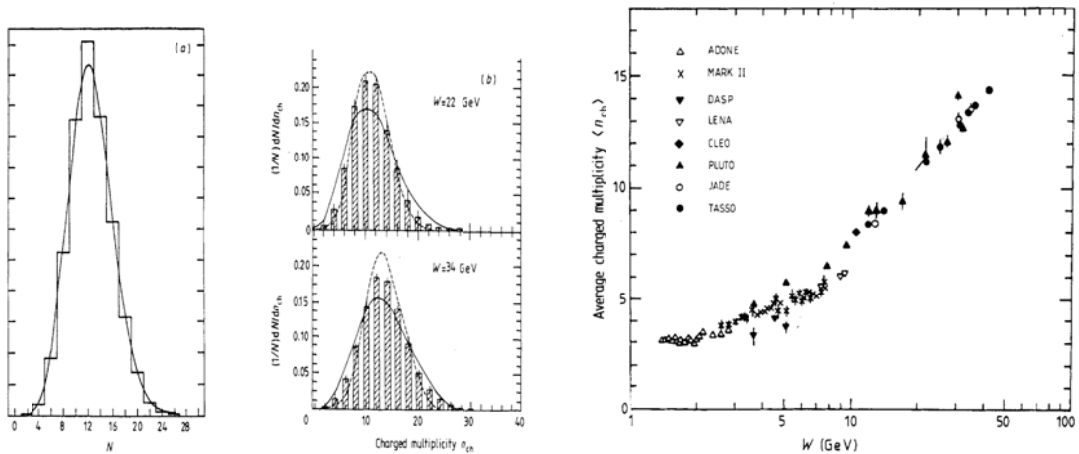


Figure 3-5: Total multiplicity distribution in  $e^+e^-$  scattering compared to a Poisson distribution (left and middle) multiplicity in  $e^+e^-$  scattering versus  $s$ . (right)

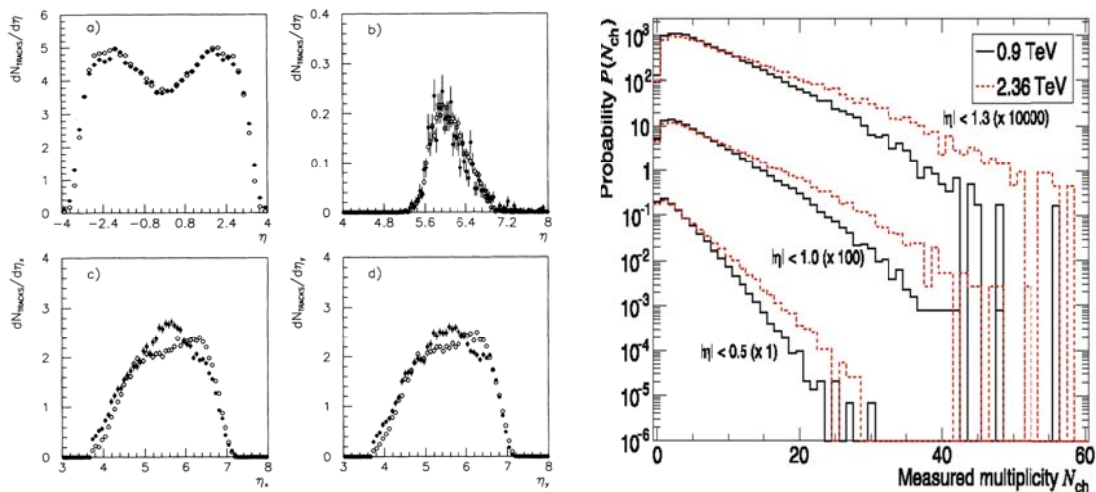


Figure 3-6: Multiplicity versus  $\eta$  at 1.8 TeV in antiproton proton collisions (left and middle) multiplicity distribution in pp collisions at LHC.

As the particle production via the string model leads to approximately constant density of particles in rapidity, mainly driven by the constant string tension, the particle multiplicity will grow logarithmically with the centre of mass energy.

Finally comparing the data at  $e^+e^-$  machines with those at  $pp$  machines one sees that the statements above are in better agreement with the  $e^+e^-$  data. The mean multiplicity grows as  $\ln\sqrt{s}$  and the multiplicity distribution behaves as a Poisson as one would expect from a single stochastic process. In hadron interactions the multiplicity grows somewhat faster and the multiplicity distribution is wider than a Poisson. This leads to the conclusion that in hadron collisions the most likely more than one production string is produced. This goes under the name of multiple parton interaction.

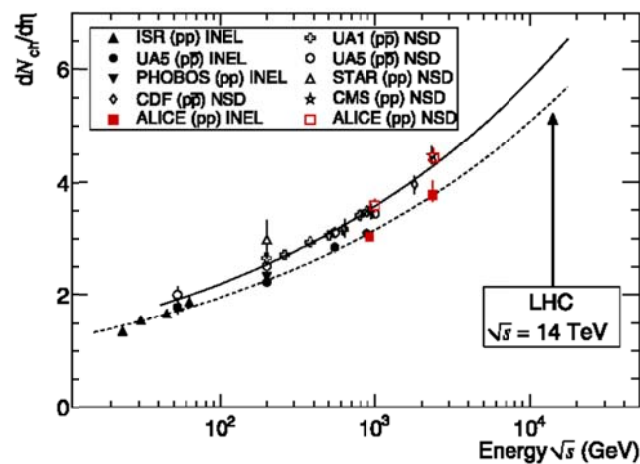


Figure 3-7: Mean differential multiplicity distribution versus  $\sqrt{s}$

**From the figure and the number of units of rapidity, calculate the multiplicity of the first interaction of a cosmic ray proton with the atmosphere (assume pp collision).**

## 4 COSMIC RAYS

Since their discovery by V. Hess in the beginning of the 20<sup>th</sup> century cosmic rays have been the subject of many investigations. They have provided the means for major discoveries such as the positron (see Figure 4-1), the muon (see Figure 4-2) and the pion (see Figure 4-3).

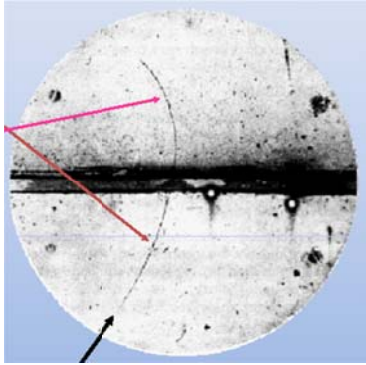


Figure 4-1: A cloud chamber picture of the discovery of the positron. From the curvature at the positions of the red arrows one concludes that the energy above the lead plate in the centre is larger than below. The particle therefore travels from below and from the direction of the magnetic field the sign of the charge is determined to be positive. The ionisation density shows the mass to be that of the electron.

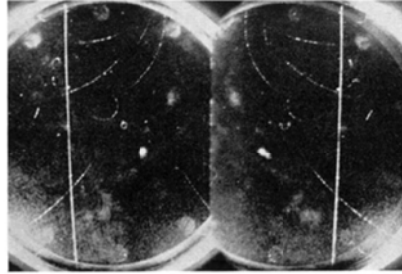


FIG. 8. Pike's Peak, 7900 gauss. A strongly ionizing particle traversing nearly vertically the full diameter of the chamber. It is probably coincident in time with the electron shower which also appears. If traveling downward it has a positive charge and an  $H\rho = 1.8 \times 10^6$  gauss cm. If it is assumed to be a proton its energy is 150 MEV and its velocity 0.5 c. The density of ionization exhibited by this track is therefore not inconsistent with the view that it represents a proton. Only a very few examples of strongly ionizing particles traversing the chamber vertically are observed.

Figure 4-2: One of the first observations of the muon in a cloud chamber exposure at the top of Pike's Peak in Colorado. The ionisation and the velocity of the particle are not consistent with the hypothesis that this is a proton, but rather something of intermediate mass. Later this mass was determined to be 106 MeV.

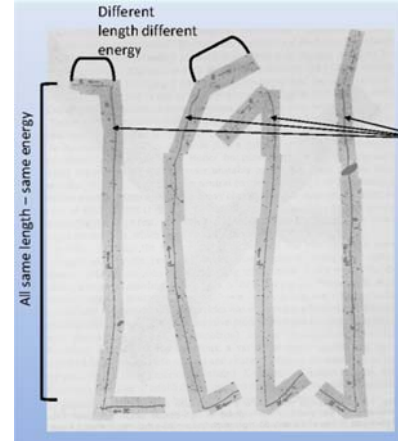


Figure 4-3: The first observation of the pion the short tracks at the bottom are the pions entering the nuclear emulsion. After stopping the pion decays at rest into a muon (arrows) and an unseen muon-neutrino. The energy of the muon is always the same indicating a two-body decay. The muon also decays but the observed electron has varying energy, indicating the absence of at least two neutrinos.

All these particles were products of interactions of primary cosmic rays with nuclei in the atmosphere. The major components of these secondary cosmic rays are muons and neutrinos. The former are used to measure the energies of the interacting particles essentially through counting of the multiplicity arriving at the surface of the earth (see chapter aaa), while the latter have provided major evidence in the investigation into neutrino oscillations (see chapter bbb). This chapter will however be mainly concerned with the primary cosmic rays that arrive at the top of our atmosphere.

### 4.1 The spectrum

The cosmic ray spectrum as it arrives at the top of the atmosphere is shown in figure aaa. There are a few characteristics worth noting about the spectrum. First there is the almost total lack of structure. With the exception of the slight kink downward at about  $10^{15}$  eV and the slight kink upward at about  $10^{19}$  eV the spectrum can be described as a power law spectrum,  $\frac{dN}{dE} \propto E^{-\gamma}$ , with the spectral index  $\gamma \cong 2.7$  below the PeV break and  $\gamma \cong 3.2$  above. The slopes are indicated by the dashed lines. This also guides the eye to where the breaks occur. The following characteristic worth noting is that the maximum particle energy is about  $10^{20}$  eV. Just to put this in context about seven orders of magnitude larger than the

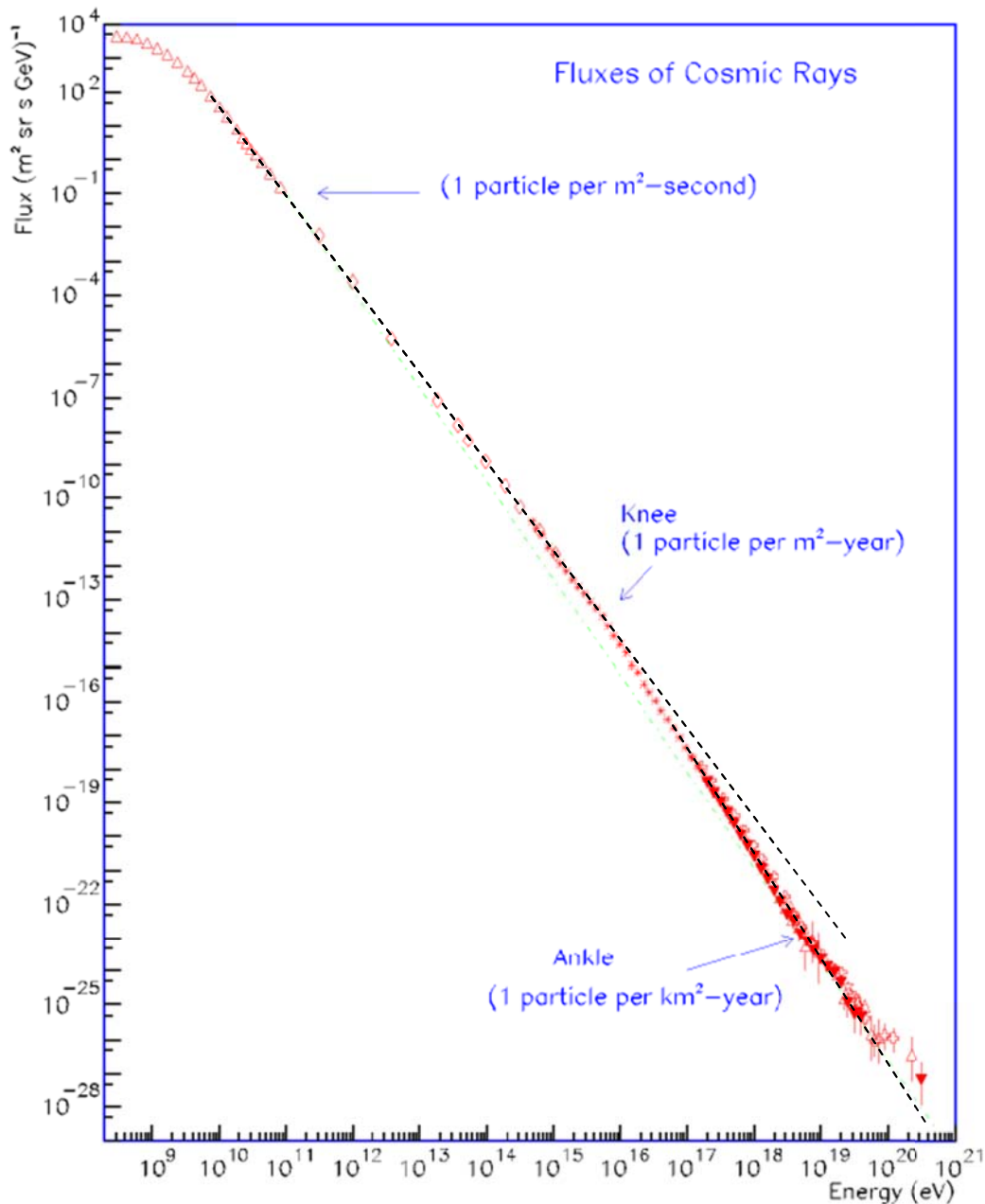


Figure 4-4: The primary cosmic ray spectrum. The intensity is shown as a function of the particle energy. The highest recorded energy was measured by the Hires experiment at  $3 \cdot 10^{20}$  eV.

LHC beam. The intensity of the cosmic rays decreases from about  $1 \text{ m}^{-2}\text{s}^{-1}$  integrated in a decade of energy centred at 100 GeV to  $1 \text{ km}^{-2}\text{year}^{-1}$  at  $10^9$  GeV. The lack of data points between about 100 GeV and 1 PeV is due to the extreme difficulty in measuring in this region.

**The flux of cosmic rays hitting the earth is given by  $\frac{dN}{dE} = 50 \left(\frac{E}{10 \text{ GeV}}\right)^{-2.7} [\text{m}^2\text{s sr GeV}]^{-1}$  up to 107 GeV after which the slope changes to 3.2. Calculate the total energy hitting every square meter of earth per second. What is the energy density in cosmic rays in GeV/m<sup>3</sup>. How does this compare to the matter density of 1 hydrogen nucleus per cm<sup>3</sup>?**

The measurements below 100 GeV are from balloon or satellite based experiments, whereas above 1 PeV the measurements of extensive air-showers are done in ground based arrays

covering up to 3000 km<sup>2</sup>. The question is what type of particles are the cosmic rays and whence do they come. To do this we first investigate what is called the chemical composition

## 4.2 Chemical composition

Figure 4-5 shows the low energy part of the cosmic ray spectrum differentiated for different nuclei. The hydrogen nucleus (the proton) has the highest intensity followed by the <sup>4</sup>He nucleus. Helium has abundance in the cosmic rays of about 7% of hydrogen. And Fe nuclei are about a factor of 5000 less abundant than hydrogen.

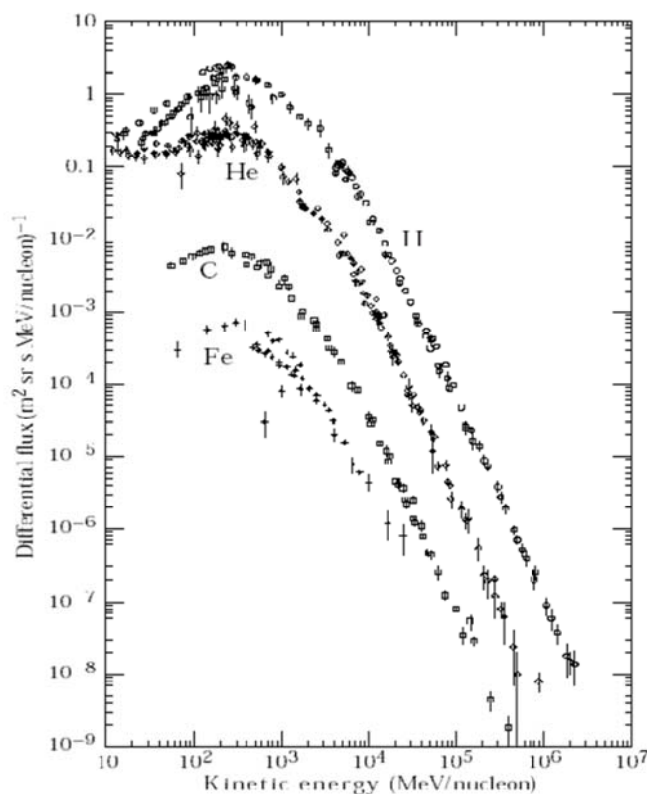


Figure 4-5: The cosmic ray spectrum differentiated according to nucleus type. Note that the intensity is shown as a function of energy per nucleon.

In the figure the intensity is plotted as a function of the energy/nucleon rather than total kinetic energy. When this is plotted as a function of the nucleus energy then the curve moves to the right and down by the factor equal to the number of nucleons. The total integral remains the same, and so the picture is more illustrative the way it is plotted here. The fact that helium is 7% by number indicates that it is about 22% of the total cosmic ray flux by mass is helium. This is in approximate agreement with the mass fraction of Helium in the Universe.

The rigidity of all the particles is equal at equal energy per nucleon, so the fact that all curves turn over at the same place is indicative that the turnover is caused by magnetic fields. Furthermore the rate below the turnover turns out to be very sensitive to the solar activity and so one concludes that the local solar magnetic fields are responsible for the turnover.

The measurement of the chemical composition of the cosmic rays has relied primarily on flying apparatus to the top of the atmosphere in balloons. This severely restricts the mass and the power consumption of the equipment. Most instruments are in principle the same and rely on a measurement of the total energy or momentum together with a measurement of the velocity of the particle. The total energy is measured by means of calorimetry and the momentum by deflection in a magnetic field. For the measurement of the velocity either Cherenkov radiation or differential energy loss is used. Figure 4-6 shows a schematic view of a typical balloon experiment.

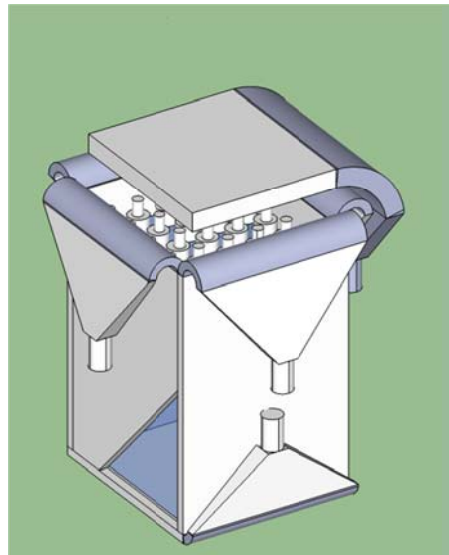


Figure 4-6: Schematic (cut open) view of balloon experiment, showing a NaI detector for the energy measurement surrounded by veto counters and above the scintillator for the measurement of the  $dE/dx$ .

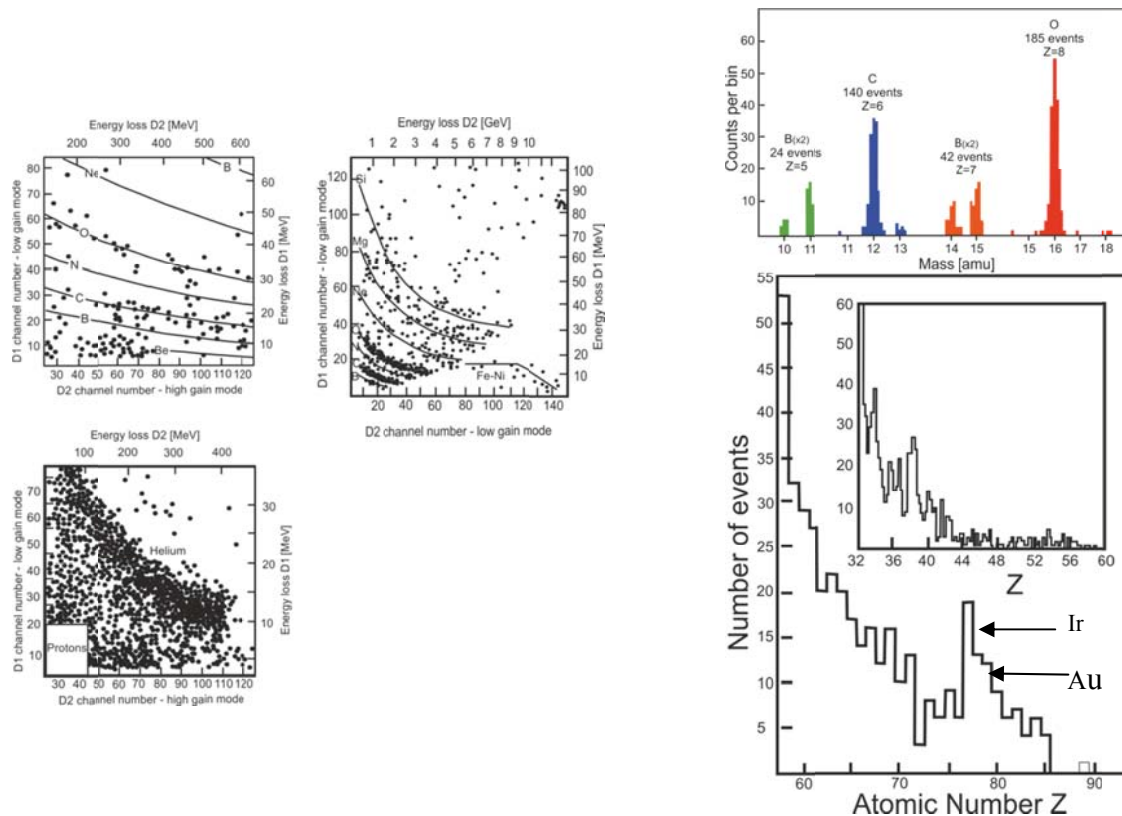


Figure 4-7: Measurements from the OGO-I satellite experiment using the  $dE/dx$  and total energy technique. Bottom left the readout gain for both detectors are high as the  $dE/dx$  scales with  $z^2$  and the energy measurement with  $A$ . Therefore protons and Helium give only small signals. In the other two plots the gains are varied to highlight different parts of the spectrum. The extracted spectra are presented on the right.

Any particle entering from above will pass through the scintillator counter leaving behind the ionisation energy as given by the Bethe-Bloch energy loss formula:

$$-\frac{dE}{dx} = Kz^2 \frac{Z}{A\beta^2} \left[ \frac{1}{2} \ln \frac{2m_e\beta^2\gamma^2 T_{max}}{I^2} - \beta^2 - \frac{\delta}{2} \right] \quad (4-1)$$

Where  $K$  is a proportionality constant,  $z$  is the charge of the projectile,  $Z$  and  $A$  are the charge of the material nucleus and its atomic number,  $\beta$  is the velocity of the projectile,  $\gamma$  its Lorentz factor,  $T_{max}$  is the maximum energy transfer to an electron in the material,  $I$  is the effective ionisation potential of the material and  $\delta$  is a factor that compensates the first term for dense materials. The total energy measured in the calorimeter is the kinetic energy of the particle,  $E_{meas} = (\gamma - 1)A_{proj}$ . Each measurement translates directly to a measured pulse height, so, plotting the one against the other, bands will appear for specific masses. Figure 4-7 shows the measurements done by the OGO-I satellite experiment. In the right panel the intensities measured in cosmic rays are given as a function of the atomic number of the projectile. It is clear that almost every nucleus present on earth is also present in cosmic rays.

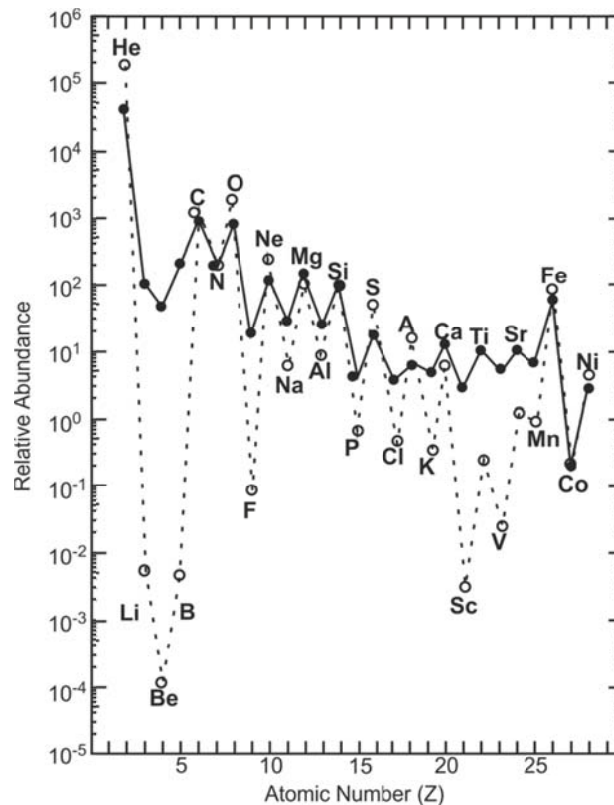


Figure 4-8: The total intensity relative to the hydrogen intensity for the nuclei up to Ni. The drawn line is the intensity observed in cosmic rays. The dashed curve shows the concentration measured in interstellar gas.

The figure shows the intensity measured for very large nuclei and there is a significant rate at the point of Iridium. This is one of the strange observations that even though interstellar gas contains significant amounts of this nucleus as do the cosmic rays, the concentration here on earth is significantly smaller. The fact that Iridium turned up in the

stratum of the earth at the point when the dinosaurs became extinct was one of the major pieces of evidence for the meteor theory for the extinction.

The total spectrum up to Nickel is given relative to hydrogen in Figure 4-8. The solid line shows the intensities in cosmic rays whereas the dashed curve gives the concentrations in interstellar gas. There are a few things to observe in the figure. There is an odd even effect in the intensity. Nuclei with an even number are more abundant than those with an odd atomic number. This effect is less pronounced in the cosmic rays than in the interstellar gas. Next the nuclei Li, Be and B and the series between Ca and Fe are much more abundant in cosmic rays than interstellar matter. So the major conclusion is that cosmic rays are very much like interstellar matter. The odd even effect is due to the fact that nuclei with even atomic number are more tightly bound, and so will occur more often as fusion products in stars. Li, Be and B on the other hand are relatively unstable and are easily converted to heavier elements in the stellar fusion processes.

The fact that these do appear in cosmic rays can be ascribed to the process of spallation whereby the accelerated cosmic rays in the C, N, O region collide with interstellar gas and split into lighter elements. The same is true for the series just below the Fe peak. These will turn out to be the products of Fe spallation.

### 4.3 Propagation

We can describe the propagation of the cosmic rays through our galaxy in terms of a diffusion equation. In principle we can have diffusion in space and in energy furthermore we can have a source of particles or a loss of particles due to for instance decay or spallation.

We will give a quick derivation of the diffusion equation and then use a simplified version to estimate the effects of spallation on the chemical composition of cosmic rays. Looking at

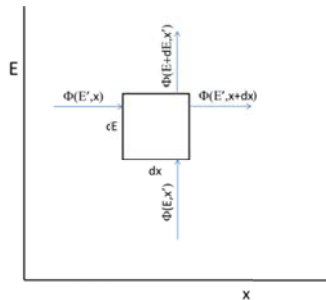


Figure 4-9: Definition of the phase-space element in energy and  $x$  space.

Figure 4-9, we can define the change of the density in the phase space element

Figure 4-9 and defining the number of particles at time  $t$  in the phase space  $[x, x + dx]$  and  $[E, E + dE]$  as  $N(E, x, t)$ , we can write the rate of change in the box as

$$\frac{d}{dt}N(E, x, t) = [\varphi_x(E, x, t) - \varphi_x(E, x + dx, t)]dE + [\varphi_x(E, x, t) - \varphi_x(E + dE, x, t)]dx + Q(E, x, t)dEdx \quad (4-2)$$

With  $Q$  denoting the rate of production at time  $t$  per unit of phase space in  $x$  and  $E$ , or

$$\frac{d}{dt}N(E, x, t) = -\frac{\partial \varphi_x}{\partial x} - \frac{\partial \varphi_E}{\partial E} + Q \quad (4-3)$$

Where  $\varphi_x$  is the flux of particles in the energy interval  $dE$  at  $E$  passing through the position interval  $dx$  at point  $x$ . The flux  $\varphi_x$  can be written in terms of the diffusion coefficient  $D$

$$\varphi_x = -D \frac{\partial N}{\partial x} \quad (4-4)$$

So equation (4-3) becomes

$$\frac{dN}{dt} = D \frac{\partial^2 N}{\partial x^2} - \frac{\partial \varphi_E}{\partial E} + Q \quad (4-5)$$

Which can be generalised to three dimensions

$$\frac{dN}{dt} = D \nabla^2 N - \frac{\partial \varphi_E}{\partial E} + Q \quad (4-6)$$

If the energy loss of the particles can be described purely as a function of the energy  $-\frac{dE}{dt} = b(E)$  we can then write

$$N(E) \frac{dE}{dt} = \varphi_E = -b(E)N(E) \quad (4-7)$$

And so we finally arrive at

$$\frac{dN}{dt} = D \nabla^2 N - \frac{\partial}{\partial E} [b(E)N(E)] + Q(E) \quad (4-8)$$

With the help of this general equation we can now start to attack the problem of spallation. We will first attack the problem of the light elements Li, Be and B, which we will assume are the spallation products of the elements C, N and O. We will simplify things a little so we put together the spallation parents and call these the M sample and the daughters the L sample.

We now modify the equation to be dependent on the species,  $i$ . We add a term that describes the disappearance of the species through the spallation, which we describe in terms of a spallation lifetime,  $\tau_i$ , and the creation of the species through the spallation of a heavier species,  $j$ .

$$\frac{dN_i}{dt} = D \nabla^2 N_i - \frac{\partial}{\partial E} [b(E)N_i] + Q_i - \frac{N_i}{\tau_i} + \sum_{j>i} P_{ji} \frac{N_j}{\tau_j} \quad (4-9)$$

Where the  $P_{ji}$  define the probability that when species  $j$  undergoes spallation that it will create species  $i$ .

This equation has of course too many unknowns, so we shall have to simplify things a little. We assume that we have a galaxy where no species are created. We assume that at  $t=0$  there is a certain number of species  $I$  after which there is no injection of new particles. The second assumption is that the cosmic rays are everywhere the same in the galaxy so that the diffusion

term will be zero. Finally we assume there is no energy loss before or after the spallation takes place. These assumptions are quite reasonable as we shall discover later. We also introduce the traversed matter density rather than time,  $\xi = \rho l = \rho ct$ . The equation then becomes significantly simplified.

$$\frac{dN_i(\xi)}{d\xi} = -\frac{N_i(\xi)}{\xi_i} + \sum_{j>i} P_{ji} \frac{N_j(\xi)}{\xi_j} \quad (4-10)$$

We now assume that the M sample has only losses, whereas the L sample has losses but is only fed from the M sample.

$$\frac{dN_M(\xi)}{d\xi} = -\frac{N_M(\xi)}{\xi_M} \quad (4-11)$$

$$\frac{dN_L(\xi)}{d\xi} = -\frac{N_L(\xi)}{\xi_L} + P_{ML} \frac{N_M(\xi)}{\xi_M} \quad (4-12)$$

Equation (4-11) is solved straightforwardly:

$$N_M(\xi) = N_M(\xi_0) e^{-\frac{\xi}{\xi_M}} \quad (4-13)$$

And we rewrite equation (4-12) as

$$\frac{d}{d\xi} \left[ e^{\frac{\xi}{\xi_L}} N_L(\xi) \right] = \frac{N_M(\xi)}{\xi_M} P_{ML} \left[ e^{\left( \frac{\xi}{\xi_M} - \frac{\xi}{\xi_L} \right)} \right] \quad (4-14)$$

From this we get

$$\frac{N_L(\xi)}{N_M(\xi)} = \frac{P_{ML} \xi_L}{(\xi_L - \xi_M)} \left[ e^{\left( \frac{\xi}{\xi_M} - \frac{\xi}{\xi_L} \right)} - 1 \right] \quad (4-15)$$

Table 4-1: Cross sections in mbarn for the spallation of heavy nuclei into the lighter nuclei.

Product Nucleus	Z	A	Parent Nucleus			
			<sup>11</sup> B	<sup>12</sup> C	<sup>14</sup> N	<sup>16</sup> O
Lithium	3	6	12.9	12.6	12.6	12.6
		7	17.6	11.4	11.4	11.4
Beryllium	4	7	6.4	9.7	9.7	9.7
		9	7.1	4.3	4.3	4.3
		10	15.8	2.9	1.9	1.9
Boron	5	10	26.6	17.3	16.0	7.1
		11	-	31.5	15.0	12.0

The experimental result for the ratio is 0.25 which together with the spallation cross sections measured at accelerator (of course with a proton beam hitting a heavy nucleus target rather than in this case, the heavy nucleus hitting the proton target) gives a traversed matter of 48

kg/m<sup>2</sup>. Note this is not a density but rather a density multiplied by the length the particle travels.

We now turn to the heavier elements that we assume all come from the spallation of Fe. The spallation cross section of Fe is  $\sigma_{Fe} = 764$  mbarns, which translates to a value of  $\xi_{Fe} = 22$  kg/m<sup>2</sup> and given the values of table for the spallation products cross sections we find that  $\xi_{Fe} \ll \xi_{prod}$  so that we must conclude that:

$$\frac{N_{prod}}{N_{Fe}} = \frac{\left(1 - e^{-\frac{\xi}{\xi_{Fe}}}\right)}{e^{-\frac{\xi}{\xi_{Fe}}}} \quad (4-16)$$

Which, putting in the values of  $\xi_{Fe} = 22$  kg/m<sup>2</sup> and of  $\xi = 50$  kg/m<sup>2</sup>, gives a predicted value of 8.7 rather than the experimental value of 0.5. There is of course a simple explanation for this in the fact that not all particles traverse the same amount of matter. Let's look at what happens if we let one third of the Fe traverse twice the amount of matter and two thirds traverse no matter at all. Of course we have to do this for the previous result also. This gives for the one third,  $\xi = 100$  kg/m<sup>2</sup>:

$$\frac{L}{M} = 0.6$$

At this point all Fe undergoes spallation. In the two thirds case no spallation products appear and all Fe and the full M sample survives. This then gives

$$\frac{L}{M} = 0.26 \text{ and } \frac{N_{prod}}{N_{Fe}} = 0.5$$

which agrees with the data. The real situation is of course a little more complicated. The cosmic rays will turn out to come mostly from our galaxy, where they are trapped by the galactic magnetic field. There is in time a certain probability for the particles to escape. They are then lost from our measurements. This model of the cosmic rays in our galaxy is known as the leaky box model. Putting this into our diffusion equation:

$$\frac{dN}{dt} = D\nabla^2 N - \frac{N}{\tau_{esc}} \quad (4-17)$$

And setting the diffusion to zero again this leads to

$$N = N(0)e^{-\frac{t}{\tau_{esc}}} \quad (4-18)$$

or

$$N = N(0)e^{-\frac{\xi}{\xi_{esc}}} \quad (4-19)$$

The final piece of information we will extract from the chemical composition is the mean escape time. We do this by looking at radioactive nuclei. In this case there is an extra loss mechanism namely the decay of the nucleus.

**Exercise: Use the values of the ratios of nuclei and the leaky box model to determine the escape traversed matter or escape time.**

For this measurement we will use the isotope  $^{10}\text{Be}$  which has a half-life of  $\tau = 3.9 \cdot 10^6$  years. In the spallation of C, N and O Be is formed of which about 10% is  $^{10}\text{Be}$ . We assume that we are in a steady state with particles being produced through spallation and being lost by spallation or escape at the same rate. We can then write, with  $C_i = \sum_{j>i} P_{ji} \frac{N_j}{\tau_j}$  for the stable isotope:

$$-\frac{N_i}{\tau_i^{esc}} + C_i - \frac{N_i}{\tau_i^{spal}} = 0 \quad (4-20)$$

which gives a trivial solution

$$N_i = \frac{C_i}{\left(\frac{1}{\tau_i^{esc}} + \frac{1}{\tau_i^{spal}}\right)} \quad (4-21)$$

And of course for the unstable isotope we have an extra term  $-N/\tau_i^{dec}$  describing the decay. So for the radioactive isotope we have:

$$N_i = \frac{C_i}{\left(\frac{1}{\tau_i^{dec}} + \frac{1}{\tau_i^{esc}} + \frac{1}{\tau_i^{spal}}\right)} \quad (4-22)$$

Now going to the specific example of  $^{10}\text{Be}$  and the stable isotope  $^9\text{Be}$  (to make it visible we denote the isotope in brackets rather than as a subscript:

$$\frac{N(^{10}\text{Be})}{N(^9\text{Be})} = \frac{C(^{10}\text{Be})}{C(^9\text{Be})} \frac{\left(\frac{1}{\tau^{esc}(^9\text{Be})} + \frac{1}{\tau^{spal}(^9\text{Be})}\right)}{\left(\frac{1}{\tau^{dec}(^{10}\text{Be})} + \frac{1}{\tau^{esc}(^{10}\text{Be})} + \frac{1}{\tau^{spal}(^{10}\text{Be})}\right)} \quad (4-23)$$

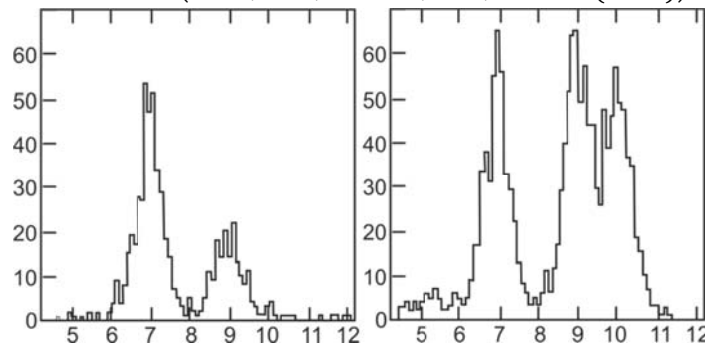


Figure 4-10: The spectrum of Be isotopes (a) in the cosmic rays and (b) in a proton  $^{11}\text{B}$  accelerator experiment using the same detection apparatus.

Simplifying with the spallation timescale larger than the escape timescale we find for the final ratio:

$$\frac{N(^{10}\text{Be})}{N(^9\text{Be})} = \frac{C(^{10}\text{Be})}{C(^9\text{Be})} \frac{\left(\frac{1}{\tau^{esc}(^9\text{Be})}\right)}{\left(\frac{1}{\tau^{dec}(^{10}\text{Be})} + \frac{1}{\tau^{esc}(^{10}\text{Be})}\right)} \quad (4-24)$$

Taking the experimental value of  $\frac{N(^{10}\text{Be})}{N(^9\text{Be})} = 0.028$  (see Figure 3-1) and  $\frac{C(^{10}\text{Be})}{C(^9\text{Be})} = 0.1$  and  $\tau^{dec}(^{10}\text{Be}) = 3.0 \cdot 10^6$  years, we can calculate the escape time:

**Exercise: Verify that the spallation timescale is indeed larger than the escape timescale. Calculate the escape timescale from the above. Given the escape timescale and the required mean traversed matter before escape (previous exercise), determine the mean matter density.**

The final conclusion we come to is that cosmic rays are almost all of Galactic origin; they are consistent with accelerated interstellar matter that undergoes spallation due to collisions with the gas in our galaxy. They have a typical escape timescale of about one million years.

**Cosmic rays are confined to our Galaxy by the Galactic magnetic field. Its magnitude is typically 10  $\mu\text{G}$  or 0.1 nT. The diameter of the galaxy is 35 kpc and 300 pc high (1pc =  $3 \cdot 10^{16}$  m). At what energy does the gyroradius of the proton equal the radius of the Galaxy (and the half-height). Can this explain the slope change?**

A final piece of evidence that the cosmic rays are of galactic origin is given by the fact that we see photons arriving from the galactic plane (see Figure 4-11). These photons are produced from Bremsstrahlung and Compton scattering and at higher energies from the decay

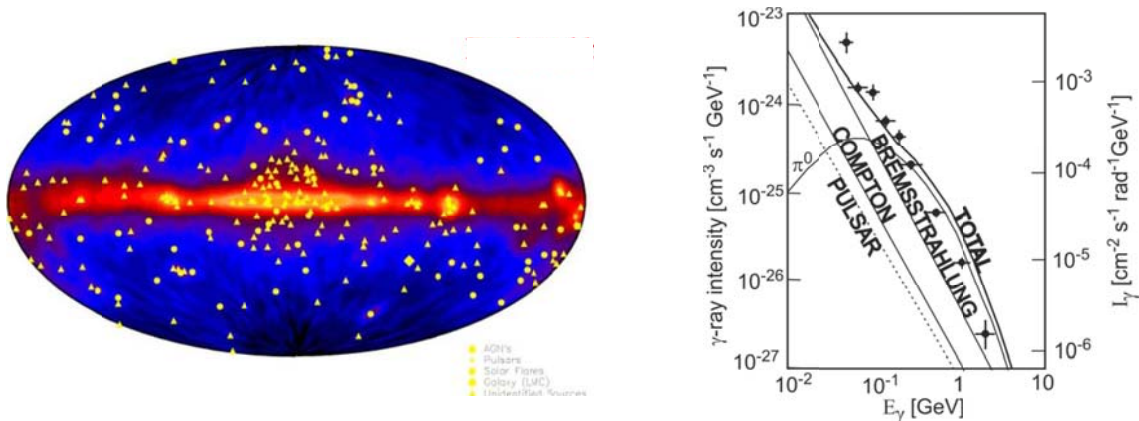


Figure 4-11:(left) Image of the gamma ray intensity of photons with an energy of more than 100 MeV. (right) The intensity, measured in the galactic plain, versus energy. The models explaining the the spectrum require a substantial contribution from  $\pi^0$  decay. The  $\pi^0$  are produced by the collisions of cosmic rays with the galactic rest gas. Above 100 MeV the spectrum is dominated by this mechanism.

of  $\pi^0$  mesons that have been produced in the interactions of cosmic rays with the galactic interstellar gas. At energies above 100 MeV this last process dominates (see Figure 4-11) and from the intensity measurements we find that the galaxy is radiating about  $10^{32}$  W due to the

$\pi^0 \rightarrow \gamma\gamma$  decay. For a relativistic proton travelling at the speed of light through a medium of protons with a number density  $N$  the probability per second of having an inelastic collision is

$$P_{coll} = \sigma_{pp}^{inel} N c = 7.5 \cdot 10^{-16} \text{ s}^{-1}$$

Where  $\sigma_{pp}^{inel} = 2.5 \cdot 10^{-30} \text{ m}^2$  and  $N = 10^6 \text{ m}^{-3}$ . In the volume,  $V$ , of the galaxy, if the density of cosmic rays with an energy  $E$  is given by  $N_{CR}(E)$  then the rate of interaction in the galaxy will be given by  $R = V N_{CR}(E) P_{coll}$ . At large enough energy isospin conservation requires that of all the pions produced 1/3 must be  $\pi^0$  mesons. Also we can assume that the inelastic collision produces mainly pions. With the empirical fact that the leading baryons take away about half the collision energy (leading particle effect) one finds that on average 1/6 of the total energy in the collision will be liberated as neutral pions and so through the pion decay to the photons. This energy can be estimated by:

$$L_\gamma = \frac{1}{6} P_{coll} V \int N_{CR}(E) E dE = \frac{1}{6} P_{coll} V \varepsilon_{CR} \quad (4-25)$$

The energy density of the cosmic rays is  $\varepsilon_{CR} = 1 \text{ MeV m}^{-3}$  and the galaxy can be approximated by a cylinder 200 pc (1 pc =  $3.08 \cdot 10^{16} \text{ m}$ ) high with a radius of 8000 pc ( $V = 2 \cdot 10^{60} \text{ m}^3$ ). So the luminosity is

$$L_\gamma = \frac{1}{6} P_{coll} V \varepsilon_{CR} = \frac{1}{6} 7.5 \cdot 10^{-16} 2 \cdot 10^{60} 1.6 \cdot 10^{-13} \text{ W} = 2 \cdot 10^{31} \text{ W}$$

which is, considering the relatively crude approximations used, in reasonable agreement with the value of the measured value.

**Exercise: Given the flux of cosmic rays in Figure 4-4 calculate the energy density of cosmic rays and verify the value given above.**

We have deduced that the cosmic rays are accelerated interstellar gas and predominantly of galactic origin. The questions we are left with are: “Where are the sources that produce the acceleration and what is the mechanism through which the acceleration takes place?”

#### 4.4 Galactic source

Given the fact that we have seen that most of the cosmic rays have galactic origin one must search for sources that can sustain a steady state of accelerated particles even though particles are lost through escape and energy is lost through radiation. It must also be possible to keep the cosmic rays captured by the galactic magnetic fields.

**Exercise: From the Lorentz force derive a formula that gives the radius of curvature  $R$  of the path that a high energy particle of charge  $e$  and momentum  $p$  will follow while in a homogeneous magnetic field  $B$ . Given the approximate galactic magnetic field strength of  $10 \mu\text{Gauss}$  or  $10^{-9} \text{ T}$  give the radius for a particle of  $p = 10^{15} \text{ eV}$ . Compare this to the height and radius of the Galaxy.**

To sustain the loss by radiation from  $\pi^0$  decay any galactic source must inject the energy of  $10^{32}W$  which in the usual dimensions used by the astronomy community is  $10^{39} \text{ erg s}^{-1}$  or  $3 \cdot 10^{46} \text{ erg year}^{-1}$ . This is a significant energy input. One of the few galactic phenomena capable of producing such energy is the Super Nova. These stellar collapses release energy of about  $3 \cdot 10^{53} \text{ erg}$  in neutrinos from the transformation  $p + e \rightarrow n + \nu_e$ . In addition the kinetic energy of the ejected matter amounts to  $10^{51} \text{ erg}$ . The radiation that is released is about  $3 \cdot 10^{49} \text{ erg}$ . Supernovae happen at roughly a rate of one per galaxy per 100-200 years. The total energy transferred to the accelerated particles must therefore be about  $3 \cdot 10^{48} \text{ erg}$  in order to sustain the interaction losses in the cosmic rays. The ejected matter is the most interesting possibility to produce acceleration as it acts as a shockwave travelling at a speed of roughly  $10000 \text{ km s}^{-1}$ . The acceleration mechanism must be quite efficient as about 3‰ of the released energy in the ejected material must be transformed into accelerated cosmic rays.

## 4.5 Acceleration

The supernova remnants in our galaxy are thus perfect candidates for the sources of high energy cosmic rays. The acceleration mechanism that we will investigate is the shockwave acceleration or first order Fermi acceleration. The idea is that the acceleration is a stochastic process and by repeating the same acceleration many times extremely large energies can be reached. The assumption we make is that we have a repeated process that each time it occurs gives an increase in energy given by

$$\frac{\Delta E}{E} = \alpha \quad (4-26)$$

In other words the energy increase per acceleration cycle is proportional to the energy. But for each cycle there is also a probability to lose a particle from the acceleration cycle.

$$P_{esc} = (1 - \beta) \quad (4-27)$$

If we now go through  $k$  acceleration cycles the number of remaining particles in the acceleration process will be

$$N_k = N_0 \beta^k \quad (4-28)$$

And the energy of the particles will be

$$E_k = E_0 \alpha^k \quad (4-29)$$

From which it follows

$$\frac{\ln\left(\frac{N_k}{N_0}\right)}{\ln\left(\frac{E_k}{E_0}\right)} = \frac{\ln \beta}{\ln \alpha} \quad (4-30)$$

And

$$\frac{N}{N_0} = \left(\frac{E}{E_0}\right)^{\frac{\ln \beta}{\ln \alpha}} \quad (4-31)$$

This represents the number of particles that have been accelerated to energy  $E$  and are still available to be accelerated further, so

$$\int_E^\infty \frac{dN}{dE'} dE' = \left(\frac{E}{E_0}\right)^{\frac{\ln \beta}{\ln \alpha}} \rightarrow \frac{dN}{dE} = \left(\frac{E}{E_0}\right)^{\left(\frac{\ln \beta}{\ln \alpha} - 1\right)} \quad (4-32)$$

The final solution is very satisfying as we have ended up with a prediction of the energy spectrum of the cosmic rays that obeys a power law. The values of  $\alpha$  and  $\beta$  are unknown unless we have a model of the process.

We now turn to the actual process of shockwave acceleration. Before we get to the acceleration we have to know something about shockwaves (for an in depth description see *Landau and Lifshitz, Fluid Mechanics, Second Edition: Volume 6 (Course of Theoretical Physics)*). Shockwaves are disturbances in gasses that travel at supersonic speeds in the gas.

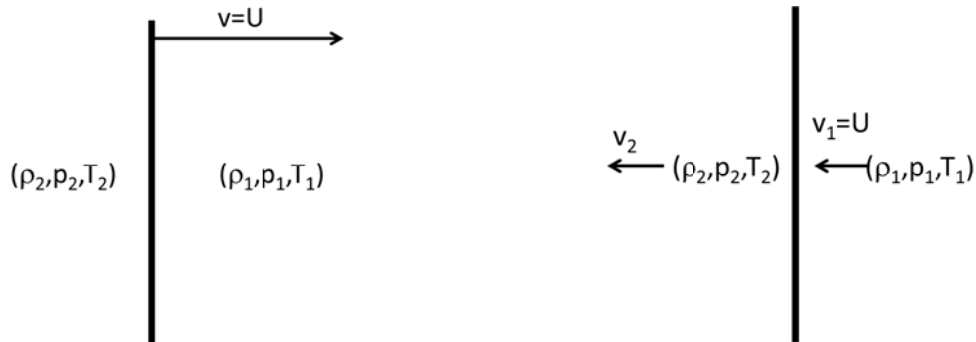


Figure 4-12: (Left) A shockwave traveling at velocity  $U$  passes through matter with density pressure and temperature  $(\rho_1, p_1, T_1)$  while the matter that has passed through the shock has  $(\rho_2, p_2, T_2)$ . (Right) The same process seen from the shockwave frame.

In Figure 4-12 a shock wave is traveling through matter with density, pressure and temperature  $(\rho_1, p_1, T_1)$  as the shock passes the density, temperature and pressure are modified through the action of the shock to  $(\rho_2, p_2, T_2)$ . The gas behind the shock will pick up some velocity. In the right panel of the figure we show the same process but seen from the shock rest frame. We now have matter passing through the shockwave, and in the process changing pressure, temperature, density and velocity. There are some conservation laws that have to be obeyed:

$$\begin{aligned} \text{Conservation of mass:} & \quad \rho_1 v_1 = \rho_2 v_2 \\ \text{Momentum flux:} & \quad p_1 + \rho_1 v_1^2 = p_2 + \rho_2 v_2^2 \\ \text{Energy flux:} & \quad \rho_1 v_1 \left(\frac{1}{2} v_1^2 + w_1\right) = \rho_2 v_2 \left(\frac{1}{2} v_2^2 + w_2\right) \end{aligned} \quad (4-33)$$

$$w_i = \varepsilon_{m,i} + pV$$

Where  $\varepsilon_{m,i}$  is the internal energy per unit mass and  $V$  is the specific volume.

From these equations we can extract information about the change of conditions before and after the shock. Using that  $w = \frac{\gamma p V}{(\gamma - 1)}$  with  $\gamma$  the ratio of specific heat at constant volume and constant pressure, and introducing the Mach number of the shock as the ratio of the shock velocity to the sound velocity of the undisturbed gas,  $M = \frac{v_1}{s_1}$  where  $s_1^2 = \gamma p_1 V_1$  we can derive the following relationships between the before and after conditions:

$$\begin{aligned}\frac{p_2}{p_1} &= \frac{2\gamma M_1^2}{\gamma + 1} \\ \frac{\rho_2}{\rho_1} &= \frac{v_1}{v_2} = \frac{\gamma + 1}{\gamma - 1} \\ \frac{T_2}{T_1} &= \frac{2\gamma(\gamma - 1)M_1^2}{(\gamma + 1)^2}\end{aligned}\quad (4-34)$$

For a Monatomic gas we have  $\gamma = 5/3$ , from which it follows

$$v_2 = \frac{1}{4}v_1 = \frac{1}{4}U \quad (4-35)$$

Transforming back to the system where  $v_1 = 0$  we see that the gas behind the shockwave is dragged along at  $3/4$  the velocity of the shockwave. Furthermore we see that the temperature behind the shockwave is very much increased. The typical sound velocity is a few hundred metres per second and the temperature  $T_1$  is a few K. This means that the temperature  $T_2$  becomes  $\sim 10^6$  K. This is high enough to ionize the gas and to create a plasma.

We now define the two Lorentz frames coinciding with  $v_1 = 0$  and  $v_2 = \frac{3}{4}U$  ( $L_1$ ) and  $v_2 = 0$  and  $v_1 = -\frac{3}{4}U$  ( $L_2$ ). If a particle in  $L_1$  travels with energy  $E$  and momentum  $p_x$  along the x-axis (perpendicular to the shock) toward the shock, then when it crosses it, it will in  $L_2$  be observed to have an energy and momentum

$$E_{L_2} = \gamma_V(E_{L_1} + p_{xL_1}\beta_V) \quad (4-36)$$

Using  $p_{xL_1} = E_{L_1} \cos \vartheta$ , we get  $E_{L_2} = \gamma_S E_{L_1} (1 + \beta_V \cos \vartheta)$ , where  $\beta_V$  is the relative velocity of the two systems,  $\beta_V = \frac{3U}{4c}$ , leading to

$$\frac{\Delta E}{E} = \beta_V \cos \vartheta \quad (4-37)$$

We assume that the particles in  $L_1$  have random directions so that  $N(\vartheta) = \sin \vartheta d\vartheta$ . The number of particles that pass the shock per second depends on  $\vartheta$ . We can thus calculate the average energy gain per crossing as:

$$\left\langle \frac{\Delta E}{E} \right\rangle = \frac{\int_0^1 c \cos \vartheta \beta_V \cos \vartheta d \cos \vartheta}{\int_0^1 c \cos \vartheta d \cos \vartheta} = \frac{2}{3} \beta_V \quad (4-38)$$

The particle is now in  $L_2$  and we assume that here the directions are randomised by turbulent magnetic fields. We can then repeat the arguments above identically for particles crossing back again from  $L_2$  to  $L_1$ . And therefore the round trip energy gain is

$$\left\langle \frac{\Delta E}{E} \right\rangle = \frac{4}{3} \beta_V = \frac{U}{c} \quad (4-39)$$

We have now an acceleration mechanism that behaves according to (4-26). We now have to find the probability that we lose particles during the process. If we have a number density,  $N_p$ , of particles that are travelling in random directions then the number of particles that travers a plane in either direction per second is given by:

$$N_{trav} = \int_{-1}^1 N_p c \cos \vartheta \, d \cos \vartheta = N_p c \quad (4-40)$$

But as the shock travels  $N_{flow} = N_p U$  flow away from the shock front. The loss probability is then:

$$P_{esc} = \frac{N_p U}{N_p c} = \frac{U}{c} \quad (4-41)$$

Using the notation of (4-26) and (4-27) we get  $\alpha = 1 + \frac{U}{c}$  and  $\beta = 1 - \frac{U}{c}$  and so for small values of  $\frac{U}{c}$  equation (4-32) becomes

$$\frac{dN}{dE} = \left( \frac{E}{E_0} \right)^{\left( \frac{\ln \beta}{\ln \alpha} - 1 \right)} = \left( \frac{E}{E_0} \right)^{\left( \frac{-U/c}{U/c} - 1 \right)} = \left( \frac{E}{E_0} \right)^{-2} \quad (4-42)$$

We have a “universal” power law for the accelerated spectrum with a spectral index that is independent of the shock velocity. So no matter how fast or slow, within reason of course, the shock wave is the same spectrum results. We have however assumed that we have a population of reasonably relativistic particles already available and we have also assumed the shock wave itself is non-relativistic. Both these assumptions are quite reasonable when talking about galactic supernovae where the shock velocities are typically a few percent of the velocity of light.

This process has to eventually cease due to several reasons. First as the energy increases in the acceleration process the particle travels a circle with an ever increasing radius. As the shockwaves have finite size the particle loss will eventually increase due to lack of magnetic confinement. The second process that starts at larger energies is the process of photopion production:



The first process leads to an energy loss of around 20% whereas the second process gives a complete loss as the neutron being neutral is no longer contained by the magnetic field. The

high temperature at the shock provides plenty of photons for this process to be relevant. Finally not only protons and nuclei will be accelerated but also electrons. These will start to emit synchrotron radiation as they are confined by the magnetic field. The energy loss per turn is given by

$$\Delta E = 8.8 \cdot 10^{-8} \frac{E^4}{R} \text{ GeV} \quad (4-44)$$

with E in GeV and R in kilometres. The synchrotron spectrum is given by

$$\frac{dN}{dE} \approx \left( \frac{E}{E_{crit}} \right)^{\frac{1}{3}} \text{ for } E \ll E_{crit} \quad (4-45)$$

and

$$\frac{dN}{dE} \approx \left( \frac{E}{E_{crit}} \right)^{\frac{1}{2}} e^{-\frac{E}{E_{crit}}} \text{ for } E \gg E_{crit} \quad (4-46)$$

and  $E_{crit} = 10^{-9} \frac{E^3}{R}$  GeV where again the energy is given in GeV and the radius of curvature in km. The maximum intensity in the energy spectrum is reached at about  $E_{crit}/3$ . The actual shape of the spectrum is given in Figure 4-13 as a function of  $\frac{E}{E_{crit}}$ . The synchrotron radiation is of course a good way to search for acceleration sites. In fact as the radiated energy increases so strongly with energy one can assume that any measured spectrum is due to the maximum contained energy. From the size of the radiating site R can be determined and from the critical energy of the spectrum E can be found. The combination of E and R then gives the magnetic field. A galactic supernova remnant is shown in Figure 4-14.

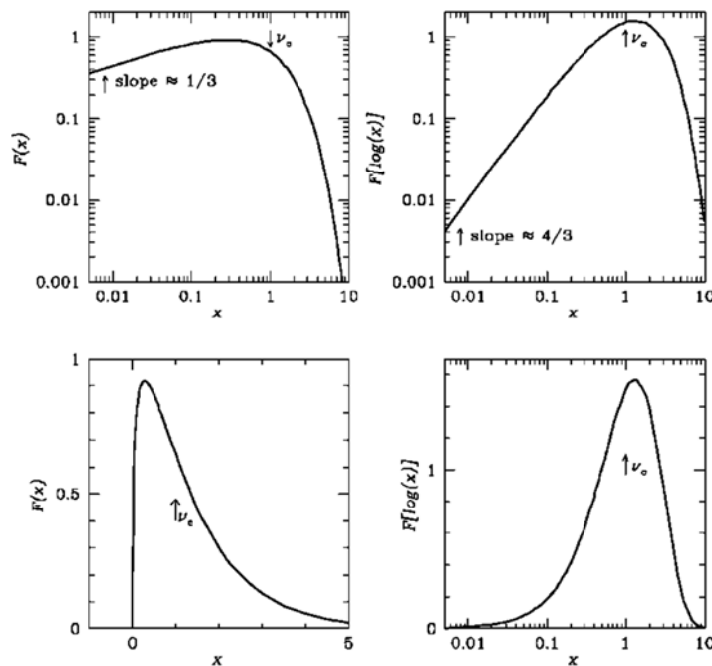


Figure 4-13: The shape of the synchrotron radiation spectrum where  $x=E/E_{crit}$

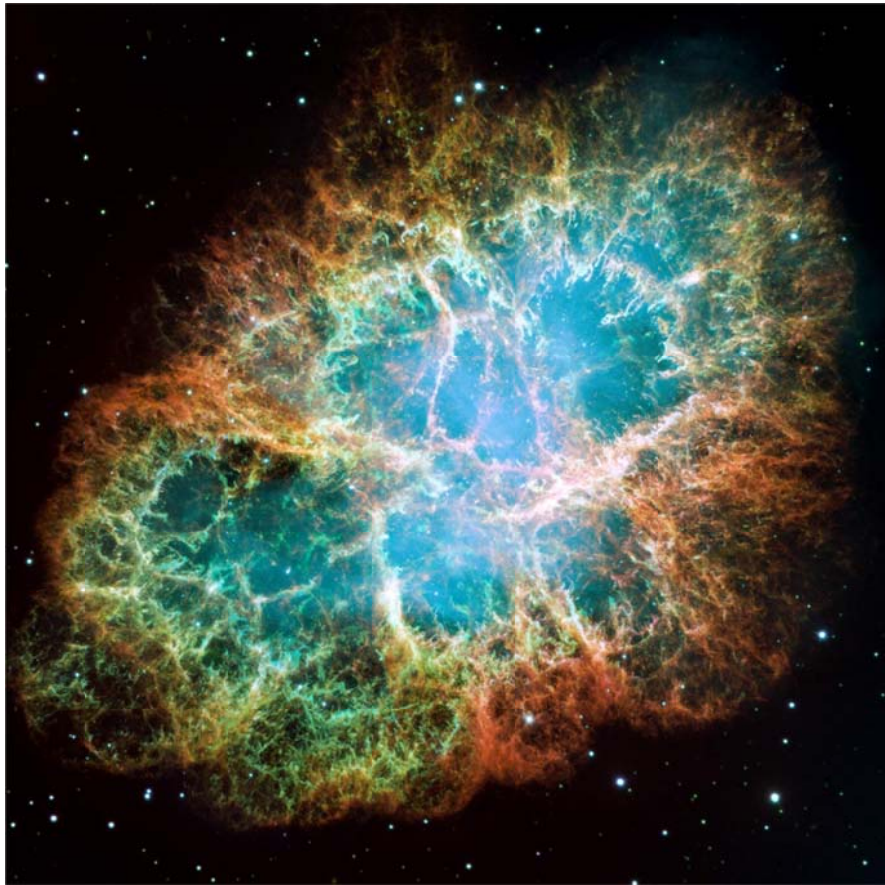


Figure 4-14: The crab nebula supernova remnant.

Assume a magnetic field of  $100 \mu\text{Gauss}$  and a velocity of the shockwave  $U=0.01c$ . At which energy will the synchrotron radiation loss per turn equal the energy gain per turn for electrons. What radius does the electron describe?

Assume the same conditions in the shock. The matter density at the shock edge is  $10 \text{ H nuclei/cm}^3$ . Given a total cross section of  $100 \text{ mbarn}$  for pp collisions, calculate the interaction length for a proton. For a proton accelerated up to energy  $E$ , calculate the total path length travelled by the particle. At what energy does the total travelled path length become equal to the interaction length?

The total photon-proton cross section is  $200 \mu\text{barn}$ . The photon density is  $10^5 \text{ photons/cm}^3$ . The photons are visible light and have an energy of  $5\text{eV}$ , at what proton energy will the centre of mass energy of a photon-proton collision be sufficient to produce a  $\Delta^+$  resonance of  $1230 \text{ MeV}$  ( $m_p=938 \text{ MeV}$ ). Give the interaction length.

## 4.6 Higher Energy

As the energy of the cosmic rays increases the containment of the interaction requires a much deeper calorimeter and in addition the flux becomes significantly smaller. The scale of the detector is then too large to allow for balloon or satellite based measurement. When observing Figure 4-4 one can note a significantly smaller number of data points between about  $100$  and  $10^5 \text{ GeV}$ .

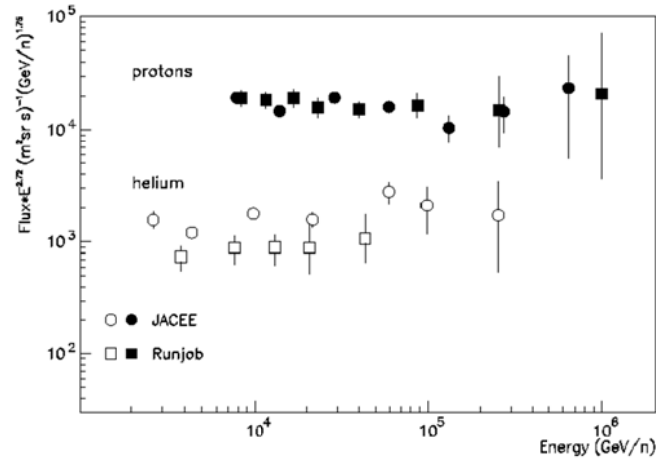


Figure 4-15: Results of the balloon experiments JACEE and Runjob, which contained stacks of nuclear emulsion as detector and were flown for exposures of one and three months above Antarctica and Siberia respectively. Note that the flux has been multiplied by  $E^{2.72}$  to produce an approximately flat spectrum. The horizontal scale is energy per nucleus.

These points were measured during long balloon flights in Antarctica and Siberia, using nuclear emulsion stacks as detector. The principle of the detection technique is a gain the same, namely measuring both  $\frac{dE}{dx}$  and total E. The separation of the He component was possible, but heavier nuclei produced too low statistics to allow for a reasonable measurement. The two measurements are in good agreement and again show a ratio of about 5% He in a predominantly H spectrum. To expand the energy range further it is clearly necessary to both expand the size of the detector and increase the running time. This was achieved by going to ground based detectors. Here the running time can be increased to several years and the area over which the experiment collects data can be enormously improved.

#### 4.7 Extended Air Showers

The ground based detectors all use the atmosphere as their primary detector. The thickness and density of the atmosphere is such that a high energy proton will interact at a height of about 10 km. In this first interaction pions are produced that then travel onward and interact again with the nuclei in the atmosphere. The pions that are produced in the secondary and tertiary interactions have less and less energy, until the point where the probability of decay while travelling the mean free path becomes substantial. At this point the pions decay into muons and muon neutrinos and each muon can in turn decay into an electron and two neutrinos. As we have seen before the multiplicity in interactions increases logarithmically with energy, while the number of secondary interactions decreases with energy. The number of muons reaching the earth can be seen as a measure for the energy of the incoming particle. If the shower were fully contained by the atmosphere then the multiplicity at the end of the shower would be a linear function of the energy. The containment is however not full and so the energy is a more complicated function of the multiplicity. This function is determined together with the spread of the shower at the surface by Monte Carlo simulation. The most likely energy of the primary is then determined from the measurement and deconvolution using the Monte Carlo results.

A second process that can be used is the neutral pion production in the primary interaction. Typically about 15-25% of the primary energy is released in the form of neutral pions that decay immediately into photons. These photons produce electron positron pairs near nuclei of the atmosphere and these positrons and electrons undergo bremsstrahlung and produce more photons. This leads to an electromagnetic shower that propagates in a very narrow core of the shower. Because the atmosphere is the equivalent of about 10 radiation lengths the very ends of the showers can reach the earth, but most of the particle production is concentrated in the first 3 radiation lengths. Here the electron density is high and the velocities of the electrons are higher than the velocity of light in the air medium. They therefore produce Cherenkov radiation in a very narrow cone around the core of the jet. In addition they can through the electronic excitation of nitrogen atoms produce fluorescence.

The two types of detectors that are used to measure the ultra high energy part of the cosmic ray spectrum are based on detecting one of these processes. The ground array experiments such as AGASA (Figure 4-16) concentrate on counting charged particles on the surface of the earth.

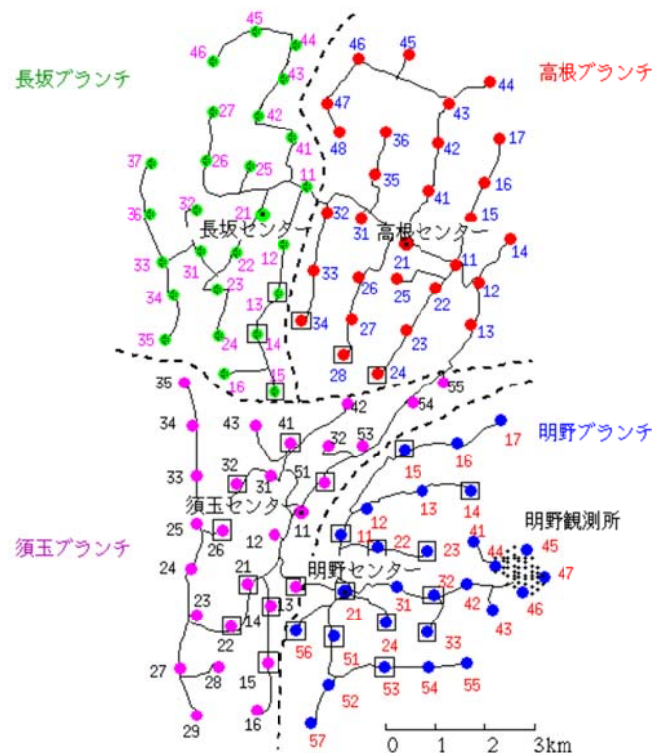


Figure 4-16: the layout of the Akeno Giant Air Shower Array. Charged particle detectors, consisting of scintillators and MWPCs with an area of about 4 m<sup>2</sup> are distributed with about 1km spacing over ~50 km<sup>2</sup>. Giant air showers typically produce particles in 6 or 7 detectors.

The other type of detector scans the night sky for images of the fluorescence created by the air shower.



Figure 4-17: The inside of the Hires detector parabolic mirrors create an image of the night sky on an array of photomultipliers. The detector consisted of two such detectors at a distance of several kilometres and imaging overlapping areas of the sky.

The results obtained by the experiments are summarized in

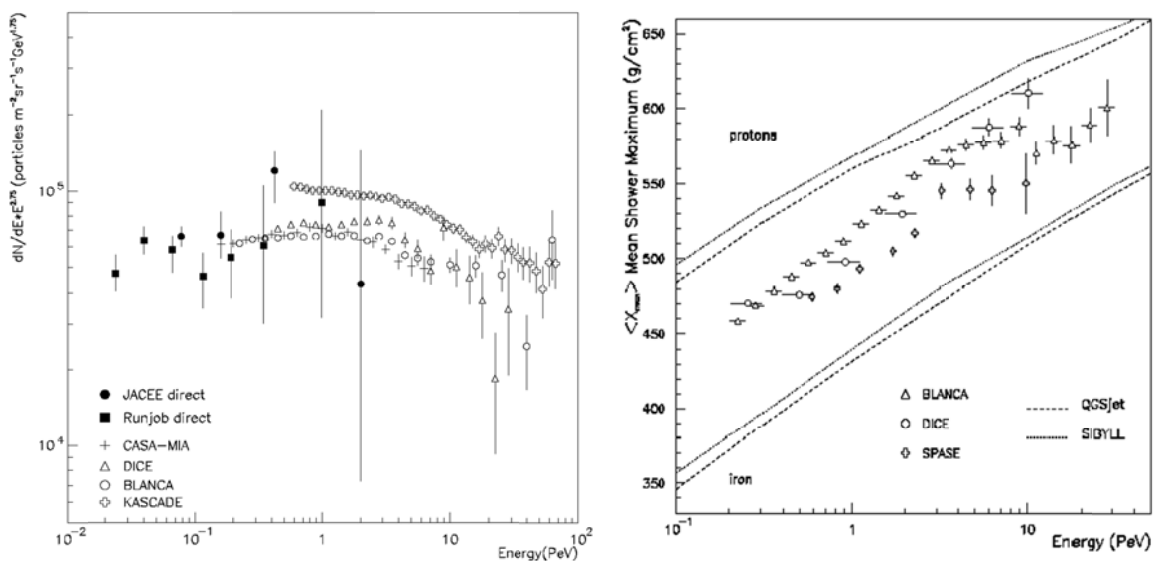


Figure 4-18: The flux of cosmic rays measured in the indicated ground based arrays, compared to the Jaycee and Runjob balloon measurements (left). The flux is again multiplied by  $E^{2.75}$ . There is reasonable agreement between experiments with the exception of cascade. Note that because of the multiplication factor a systematic difference in energy measurement of a few percent can lead to such a discrepancy. The mean depth at which the air shower occurs as a function of the cosmic ray energy (right). At around 5 PeV there is a hint of the interactions becoming more iron like.

The ground based arrays are in reasonable agreement with each other and with the balloon experiments. A possible systematic energy calibration difference of about 10% can produce the variation in the flux values as the flux has been multiplied by  $E^{2.75}$ . Also shown is the mean depth of interaction at which the interaction occurs. At the point where the flux shows a change in slope the depth measurements show an indication for the spectrum to consist more of heavy ions rather than protons. The evidence for this is not overwhelming, but it is consistent with the idea that the sources of the cosmic rays are galactic and as such limited in size and magnetic field. This limits the maximum energy for acceleration. Because of the

higher charge of the heavy ions they will be confined by the magnetic fields up to higher energies than the protons. This then translates into a larger percentage of heavy ions as first the protons run out of acceleration then the He and then in turn the heavier ions.

**Exercise:** For a given accelerator site calculate the ratio of the radius that a 1 PeV proton encribes and that of an Fe ion. If the acceleration is limited to 1 PeV give a plot showing the size of the acceleration source versus its associated magnetic field.

**Exercise:** Given a total inelastic proton-proton cross section of  $\sigma_{pp} = 30$  mbarn calculate the difference in depth between Fe and p interactions with nitrogen. Compare this with Figure 4-18. Explain the fact that both for Fe and p the depth of interaction increases with energy, even though the total cross section actually rises with energy.

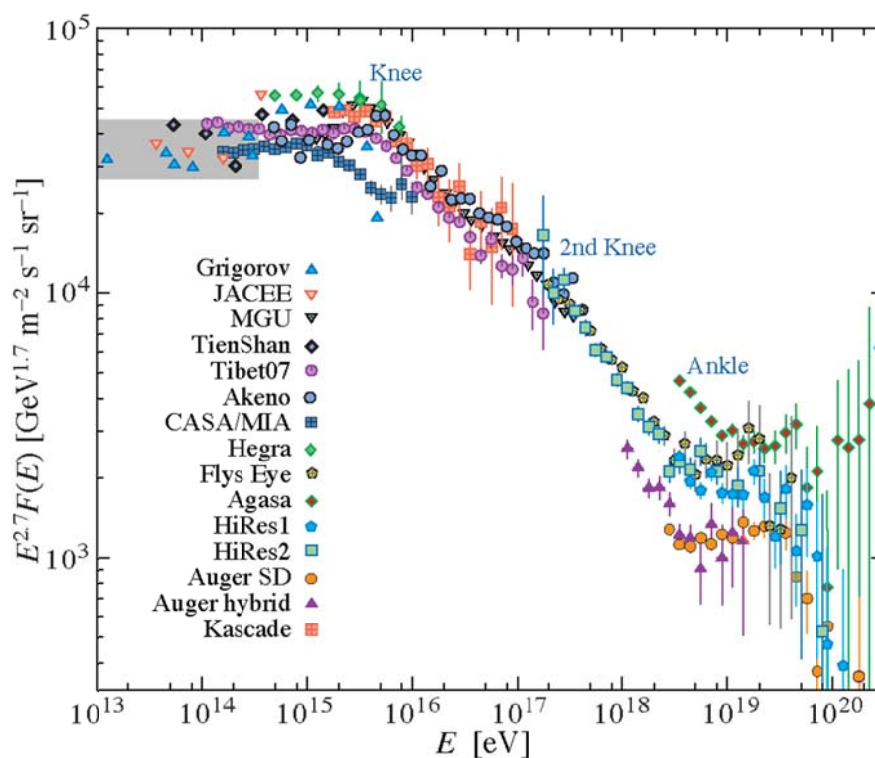


Figure 4-19: The high energy part of the cosmic ray spectrum. The differences between the different experiments are most likely due to different energy calibrations. Typical systematic errors are quoted to be at the 10–20% level. A shift in the energy scale downward by 20% is, because of the  $E^{2.7}$  factor in front of the flux, accompanied by a 60% change downward in the normalisation of the curve.

As the energy increases the intensity falls and therefore the detectors have to increase in size. This has culminated in the Pier Auger observatory in Argentina. This detector covers about 3000 km<sup>2</sup> of the high pampa at an altitude of about 2000 m. The detector is a combination of water Cherenkov detectors as a ground array and six fluorescence detectors that allow for coincidence measurement of the two types of signal. The intensity of the fluorescence signal gives a measure of the energy. It must be corrected for the distance of the detector to the shower. By measuring the same shower in at least two detectors the position of the shower in the atmosphere can be pinpointed by “triangulation”. Further coincidence with the ground array allows for a cross calibration of the energy measurement from the fluorescence intensity

and the multiplicity measurement. The latest measurements are shown in Figure 4-19 and expanded at the very highest energies in Figure 4-20.

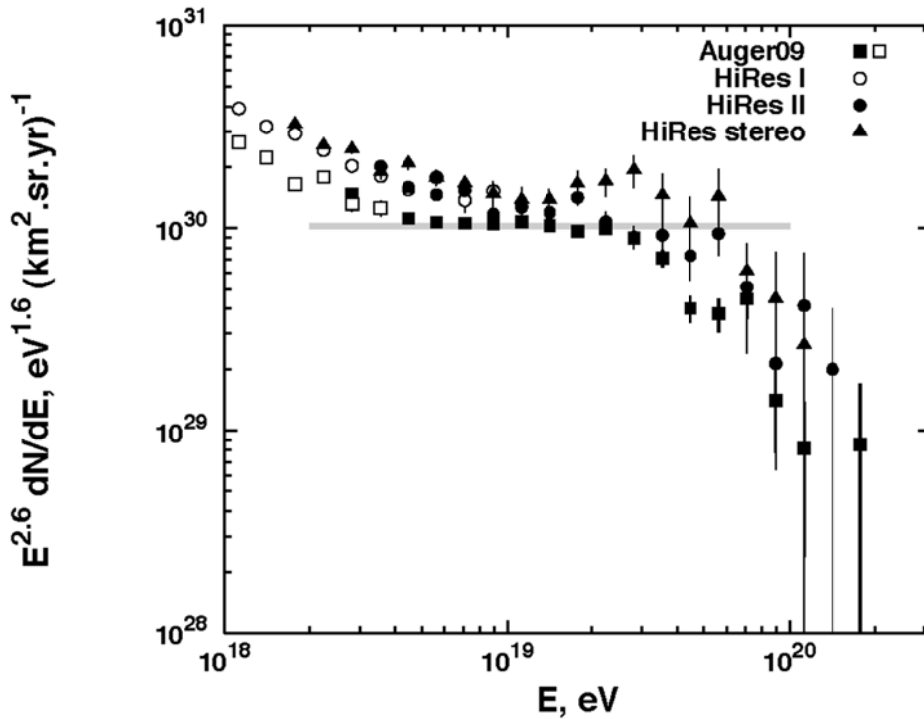


Figure 4-20: The Ultra high energy part of the cosmic ray spectrum. The most recent measurements are shown. Note the fall off in the spectrum at an energy of  $E = 10^{19.2}$  eV.

It is clear that the overall trend of all data sets is a sharper decrease of the intensity after the “knee” at about 1 PeV and a significant flattening at  $E = 10^{18.5}$  eV which at  $E = 10^{19.2}$  eV is followed by a sharp decrease. The interpretation of the last two features is an extragalactic component with a flatter energy spectrum appearing from under the galactic background. This component is then cut off by the fact that at the highest energy the cosmic rays interact with the cosmic microwave background. The mean energy of the cosmic microwave background is of the order  $10^{-4}$  eV which together with a proton energy of about  $10^{19}$  eV allows for the production of a  $\Delta$  resonance

$$p\gamma \rightarrow \Delta \rightarrow p\pi^0/n\pi^+ \quad (4-47)$$

Because the Q-value (momentum of the decay products in the resonance rest frame) of the decay is almost zero the velocity of the pion will be approximately the same as that of the proton after the decay so that

$$\frac{E_p}{m_p} = \frac{E_\pi}{m_\pi} \quad \text{or} \quad \frac{E_p}{E_p + E_\pi} = \frac{\frac{m_p}{m_\pi}}{\frac{m_p}{m_\pi} + 1} = 0.87 \quad (4-48)$$

The density of around  $400 \text{ photons/cm}^3$  and the  $\Delta$  photo-production cross section  $\sigma(\gamma p \rightarrow \Delta) = 200 \text{ } \mu\text{barn}$  translate into a mean free path of around 20 Mpc. At a distance larger than

this a proton with an energy larger than the threshold energy for D production will interact and lose 13% of its energy. When the energy has dropped below the threshold the proton can travel large distances, only losing very small amounts of energy through the process of pair production. As the source that produces such energies must be either large or have a large magnetic field and produce a significant amount of radiated energy. Such sources are possible and a small number are within the required few tens of Mpc. The possible sources are indicated in Figure 4-21. The most promising sources are the active galactic nuclei and the gamma ray bursts. It is worth noting that no galactic sources are able to provide sufficient acceleration.

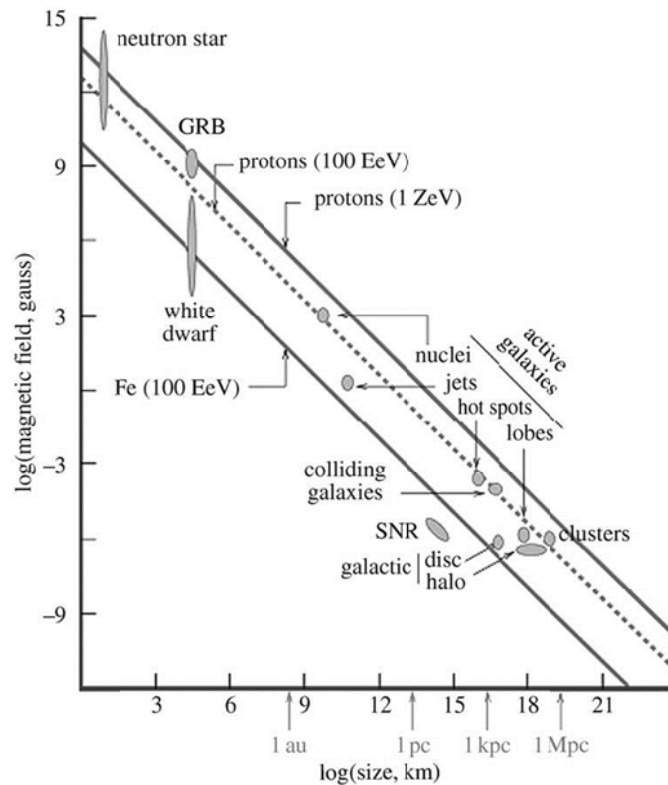


Figure 4-21: The Hillas plot where the logarithm of the size of an object is plotted against the produced magnitude of the magnetic field. The Drawn lines show the size magnetic field correlation required for acceleration to  $10^{21}$  eV and Fe nuclei up to  $10^{20}$  eV. The dashed line gives the limit for  $10^{20}$  eV protons. Known astrophysical objects are also indicated.

## 5 Nucleosynthesis

In the big bang picture of the Universe, all matter is created in a big flash of energy about  $1.5 \times 10^{10}$  years ago. From the energy particles were created and mass was formed. The expansion of the Universe is described by Einstein's general relativity and more precisely by the Friedman equation:

$$H^2 = \left(\frac{\dot{R}}{R}\right)^2 = \frac{8\pi G \rho_{tot}}{3} - \frac{Kc^2}{R^2} \quad (5-1)$$

Where H is the Hubbel constant, G is the gravitational constant,  $G = 6.7 \times 10^{-11} [\text{Nm}^2\text{kg}^{-2}]$ ,  $\rho_{tot}$  is the total mass density of the Universe and K is the curvature constant which can take on the values -1, 0 or 1.

The total mass density is either in the form of matter or radiation. As the Universe expands the matter density will decrease as  $R^{-3}$ , ie matter is conserved and the volume increases as the cube of the radius.

For radiation the "mass density" is given by the energy density divided by the velocity of light squared. This has a different behaviour to that of matter. As the length scale of the universe increases the wavelength of the light gets proportionally longer and so the energy of a photon will decrease inversely proportional to R. Combined with the constancy of the number of photons this leads to the radiation energy density ( i.e. the energy density of all relativistic particles) will decrease as  $\rho_r \propto R^{-4}$ .

At very early times we can therefore easily neglect the curvature term and use the Friedman equation in the following form.

$$H^2 = \left(\frac{\dot{R}}{R}\right)^2 = \frac{8\pi G \rho_{tot}}{3} \quad (5-2)$$

As  $\rho_r \propto R^{-4}$  it follows that

$$\frac{\dot{\rho}_r}{\rho_r} = -4 \left(\frac{\dot{R}}{R}\right) = -4 \left(\frac{8\pi G \rho_{tot}}{3}\right)^{\frac{1}{2}} \quad (5-3)$$

From which it follows by integration that

$$\rho_r c^2 = \frac{3c^2}{32\pi G} \frac{1}{t^2} \quad (5-4)$$

According to Stefan-Boltzman a photon gas has an energy density that depends on the temperature according to

$$\rho_r c^2 = \frac{4\sigma T^4}{c} = \frac{\pi^4 (kT)^4 \frac{g_\gamma}{2}}{15\pi^2 \hbar^3 c^3} \quad (5-5)$$

Where k is Boltzman's constant,  $k = 1.38 \times 10^{-31} \text{J/K}$ ,  $\sigma$  is Stefan-Boltzman's constant,  $g_\gamma$  are the number of spin-degrees of freedom of the photon and h is Planck's constant,  $h = 6.6 \times 10^{-34} \text{Js}$  and  $\hbar = h/2\pi$ .

From equations (5-4) and (5-5) one then derives a relation between temperature and time of expansion

$$kT = \left( \frac{45\hbar^3 c^5}{32\pi^3 G} \right)^{\frac{1}{4}} \left( \frac{2}{g_\gamma} \right)^{\frac{1}{4}} \frac{1}{t^{\frac{1}{2}}} \approx \frac{1.31[\text{MeVs}^{\frac{1}{2}}]}{t^{\frac{1}{2}}} \quad (5-6)$$

Or

$$T \approx \frac{10^{10}[\text{Ks}^{\frac{1}{2}}]}{t^{\frac{1}{2}}} \quad (5-7)$$

Photons are not the only relativistic degrees of freedom in the early universe. Fermions will also count. For them the energy density takes on a different form. We know that the number density as a function of energy is given by:

$$N(p)dp = \frac{g_f}{2} \frac{p^2 dp}{\pi \hbar^3 (e^{E/kT} + 1)} \quad (5-8)$$

For the situation where  $kT \gg mc^2$  so that  $E = pc$  we can use

$$\int \frac{x^3}{(e^x + 1)} dx = \frac{7\pi^4}{815} \quad (5-9)$$

To derive

$$\rho_f c^2 = \frac{7\pi^4}{815} \frac{(kT)^4}{\pi^2 \hbar^3 c^3} \frac{g_f}{2} \quad (5-10)$$

Therefore the energy density for all relativistic degrees of freedom can be derived from the formula for the photon gas by replacing  $g_\gamma$  by  $g^*$  with

$$g^* = \sum g_b + \frac{7}{8} \sum g_f \quad (5-11)$$

Where  $g_b$  is the number of bosonic spin degrees of freedom and  $g_f$  is the number of fermionic degrees of freedom. In the early times this includes all particles such as the fermions: six quarks with  $g=2$ , a number of charged leptons with  $g=2$ , a number of neutrinos with  $g=1$ , photons with  $g=2$ , three weak bosons with  $g=3$  and a Higgs particle with  $g=1$ . Where appropriate the antiparticles will also count. So we have

$$kT = \left( \frac{45\hbar^3 c^5}{32\pi^3 G} \right)^{\frac{1}{4}} \left( \frac{2}{g^*} \right)^{\frac{1}{4}} \frac{1}{t^{\frac{1}{2}}} \quad (5-12)$$

Or rewriting

$$H(t) = \frac{\dot{R}}{R} = -\frac{\dot{\rho}}{4\rho} = \frac{1}{2t} \quad (5-13)$$

$$H(T) = \left( \frac{4g^*\pi^3 G}{45\hbar^3 c^5} \right)^{\frac{1}{2}} (kT)^2 \quad (5-14)$$

So depending on the number of relativistic degrees of freedom we have a relationship between temperature and time. We will now turn to the process of nucleosynthesis and by using the evolution of temperature with time that varies depending on the number of degrees

of freedom derive the dependence of the present Helium abundance as a function of the number of neutrinos.

## 5.1 Proton to Neutron ratio

According to the formulae derived in the previous chapter at about 1 ms after the Big Bang the temperature will have dropped below 100 MeV (this is of course dimensionally incorrect what is really meant is that  $kT < 100$  MeV, but it has become jargon to assume  $k=1$ ). At this point the only hadrons that will remain are the proton and neutron. All other hadrons have lifetimes much shorter than 1 ms and the temperature is insufficient to sustain the inverse of the decay of massive hadrons. In principle their anti-particles are also present but they will annihilate with most of the protons and neutrons. The fact that they do not remove all protons and neutrons is the subject of a different lecture. There are several interactions that determine the ratio of neutrons to protons

$$\nu_e + n \leftrightarrow e^- + p \quad (5-15)$$

$$\bar{\nu}_e + n \leftrightarrow e^+ + p \quad (5-16)$$

$$n \rightarrow p + e^- + \bar{\nu}_e \quad (5-17)$$

As they are non relativistic at these temperatures the ratio of their numbers will be given by the ratio of their Boltzman factors:

$$\frac{N_n}{N_p} = \frac{e^{-M_n c^2 / kT}}{e^{-M_p c^2 / kT}} = e^{-Q/kT} \quad (5-18)$$

with  $Q = 1.293$  MeV.

For the interactions (5-15) and (5-16) their rate will depend linearly on the density and these weak interactions depend quadratically on the relative energy and so on the temperature. As the energy of the photons and so the temperature depends on  $R$  as  $R^{-1}$  and the density has a  $R^{-3}$  dependence the interaction rate depends on the temperature as

$$W \propto T^5 \quad (5-19)$$

The expansion rate however depends on the temperature as

$$H(T) \propto (g^*)^{\frac{1}{2}} (T)^2 \quad (5-20)$$

So that the expansion rate will at a certain time become larger than the interaction rate. At this point the interactions will cease, or freeze out. This happens at  $kT = 0.8$  MeV assuming the relativistic degrees of freedom associated with three families of neutrinos. At this temperature the neutron to proton ratio is

$$\frac{N_n(0)}{N_p(0)} = e^{-1.293/0.8} = 0.2 \quad (5-21)$$

From this point on only neutron decay will take place. The neutron has a lifetime of  $\tau = 887$  s. so that the neutron to proton ratio will evolve as:

$$\frac{N_n(t)}{N_p(t)} = \frac{0.2e^{-t/\tau}}{1.2 - 0.2e^{-t/\tau}} \quad (5-22)$$

## 5.2 Deuterium production

There is an equilibrium process for the production and disintegration of Deuterium



The binding energy of Deuterium is 2.2 MeV and so the disintegration requires the density of photons with energy larger than 2.2 MeV to be the same or larger than the density of protons and neutrons. As the ratio of photons to protons is of the order  $10^{10}$  the process only departs from equilibrium at a temperature that is significantly lower than  $kT = 2.2 \text{ MeV}$ . This occurs when the density of photons with energy above 2.2 MeV becomes comparable to the deuterium density. This happens at  $kT = 0.0475 \text{ MeV}$ . As soon as Deuteron disintegration stops other processes can start forming heavier nuclei:



Using (5-12) with  $g^*$  given by the photons (2), electrons (14/8), positrons (14/8) and neutrinos ( $N_\nu \cdot 7/8$ ), the time at which the deuterium disintegration stops is  $t = 380 \text{ s}$  for  $N_\nu = 3$ . The ratio of neutrons to protons is then modified to

$$\frac{N_n(t)}{N_p(t)} = r = \frac{0.2e^{-380/887}}{1.2 - 0.2e^{-380/887}} = 0.122 \quad (5-28)$$

The ratio of He to H is then given by (assuming all neutrons end up in  ${}^4\text{He}$ )

$$\frac{N_{\text{He}}}{N_{\text{H}}} = \frac{\frac{1}{2}N_n}{N_p - \frac{1}{2}N_n} = \frac{r}{2 - r} = 0.065 \quad (5-29)$$

So that the mass density ratio is given by

$$\frac{M_{\text{He}}}{M_{\text{H}}} = \frac{N_{\text{He}}}{N_{\text{H}}} = 0.26 \quad (5-30)$$

The dependence on the photon to proton ratio is shown in Figure 5-1. The measured Helium abundance and the ratio of photons to protons allows for a limit of four to be set on the number of light neutrino species.

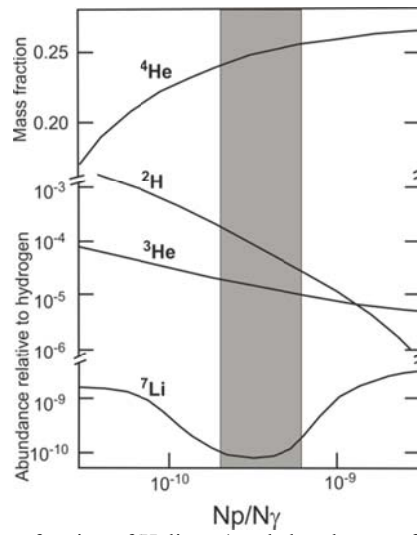


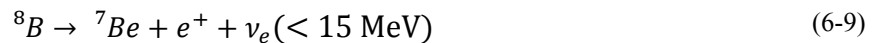
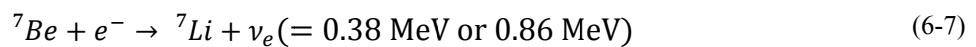
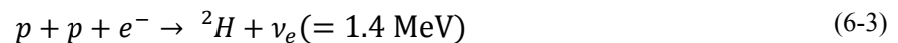
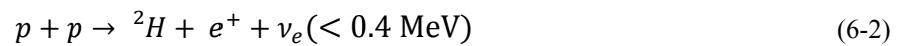
Figure 5-1: mass fraction of Helium-4 and abundances of other light elements.

## 6 Neutrino Oscillations

The first attempt at using neutrinos to investigate extraterrestrial objects was done by Ray Davis in the 1950's. The model for the energy production in the Sun had just been built based on the nuclear fusion process. This process involved a large number of successive fusion processes beginning with the main contributor the fusion of two protons to a deuterium nucleus via:



The neutrino that is emitted in this process has an energy of up to 0.46 MeV. This energy is extremely difficult to measure experimentally. However the production of Deuterium makes it possible that further fusion processes take place and in some of these processes or in the decay of the produced nuclei neutrinos of larger energy are produced. This makes these neutrinos somewhat easier to detect. The processes that take place in the Sun are the following:



Especially the processes (6-7) and (6-9) are interesting as they produce neutrinos energetic enough to be detected. Figure 6-1 shows the expected spectrum of neutrinos from the Sun.

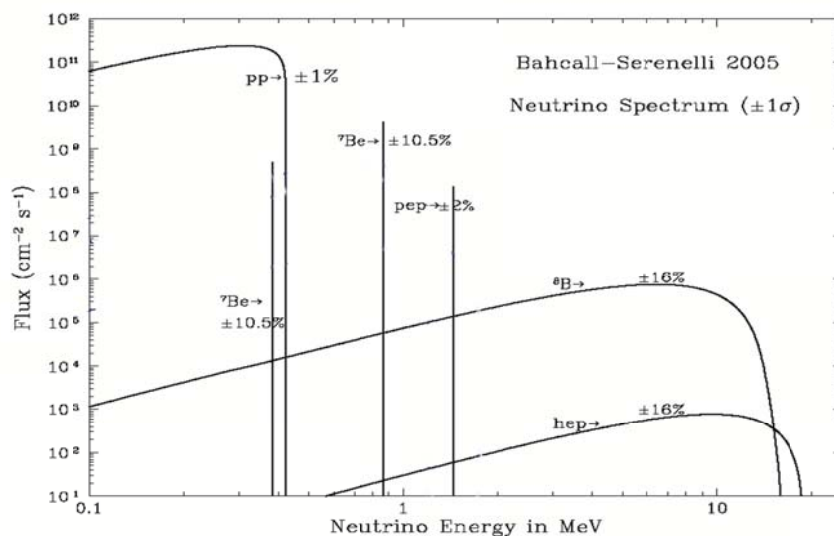


Figure 6-1: The expected neutrino energy spectrum from the Sun.

## 6.1 Homestake, SAGE and Gallex

The Davis experiment used a large volume of perchloroethylene using the capture process on the chlorine nuclei to allow for the detection of the neutrinos. The reaction used was:



This reaction is sensitive to neutrinos down to an energy of 0.8 MeV and so is predominantly sensitive to the decay of  ${}^7\text{Be}$ . The expected rate in the 100,000 gallon of cleaning fluid was a few tens per week. The Argon was harvested by bubbling ultra pure Helium through the tank and measuring the decay of the Argon nuclei by using the gas in a Geiger counter.

The experiment was able to measure a flux of neutrinos in the detector at the level of  $\varphi \times \sigma = 2.55 \pm 0.17 \pm 0.15$  [SNU] where the Solar Model predicted  $\varphi \times \sigma = 7.5 \pm 1.0$  [SNU]. The mnemonic SNU stands for Solar Neutrino Unit and is defined as the capture rate in an equipment equal to  $10^{-36}$  per second per nucleus in the detector and is therefore equal to the flux from the sun times the cross section of the interaction used to measure the neutrinos. The lack of neutrinos was first attributed to the experimental apparatus or the Solar Model. After all, the predicted flux from the model for varied proportional to the core temperature of the Sun to the 10<sup>th</sup> power, and of course extracting a handful of Argon atoms from a vat of  $10^{31}$  perchloroethylene molecules with know efficiency was considered rather too ambitious.

The Solar model was refined significantly and measurements of Solar seismology determined the core temperature to a few percent making the predictions of the rates of the Boron decay accurate to about 30% and that of the Beryllium decay to about 20% and the rate from the pp fusion is accurate to better than 10%. The search was therefore on for more accurate measurement techniques. The one concentrated on a similar technique as employed in the Homestake experiment, but replaced the Cl nucleus by a Ga nucleus. The remainder of the experiment is similar in that the produced Ge atoms are washed out of the Ga with hydrogen peroxide and a destilation process then concentrates the number of Ge atoms and after several more concentration processes, the Ge is fed into a proportional chamber where the decay of the nucleus is measured. Again a few tens of Ge atoms are produced per month. The rection used is:



The big advantage of this reaction is the low threshold of 0.3 MeV. With this experiment one is thus sensitive to the pp fusion process of the Sun. The results after a very large nmbre of calibration checks was that the measured rate was  $\varphi \times \sigma = 67.2 \pm 7.0 \pm 3.5$  [SNU] compared to the predicted rate of  $\varphi \times \sigma = 129.0 \pm 4.0$  [SNU] so rougly a factor of two too low.

## 6.2 Water detectors

In the beginning of the 1980s there was great interest in the measurement of the proton lifetime, because of the SU(5) model of Grand Unification. The SU(5) symmetry group is the smallest group that incorporates the Weak-EM SU(2) and the Strong SU(3) groups. The

unification was determined to take place at an energy scale of around  $10^{15}$  GeV and by design incorporated a connection between the quark sector and the lepton sector of the particle physics Standard Model. The intermediate bosons of the theory were capable instigating quark-lepton transitions and so predicted the decay of the proton. The lifetime determined from the model is dominated by the massive propagators with a mass around  $10^{15}$  GeV was in the range  $10^{32}$ - $10^{34}$  years. This is a value that is within the realms of measurement.

### 6.3 Water detectors: IMB and Kamiokande

Two detectors with essentially the same design were built for the measurement of proton decay: the Irvine-Michigan-Brookhaven experiment and the Kamioka Nucleon Decay Experiment. The search for the nucleon decay was performed in the predicted decay channel:



The decay of the  $\pi^0$  yielded two photons that then produced an electromagnetic shower of electrons and positrons that produced Cherenkov light in the water of the detectors. The light was detected with photomultipliers on the wall of the water tank (see Figure 6-2). The light signal from the  $\pi^0$  was produced back-to-back with a similar shower produced by the positron. This signature was the major way to separate the signal from the background caused by the interaction of atmospheric neutrinos in the detector. These tended to produce only single sided events (see Figure 6-2).

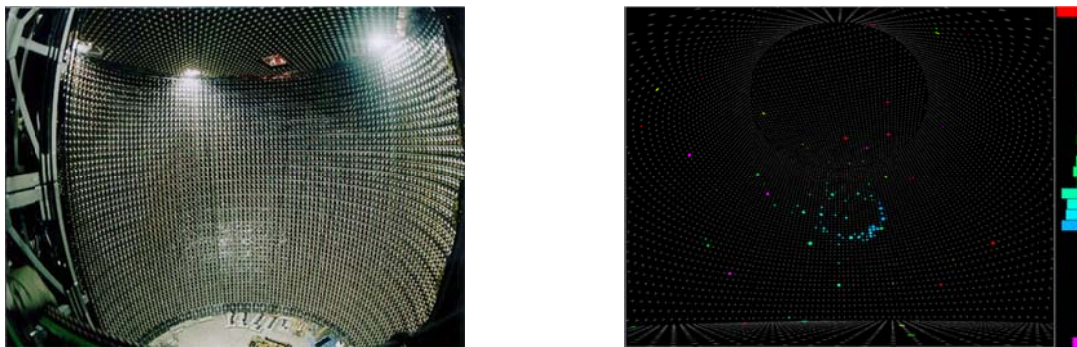


Figure 6-2: Left the photomultipliers connected to the wall of the Kamioka water tank used for the measurement of proton decay. Right a background event caused by the interaction of a neutrino in the water of the tank. The ring is a reflection of the emission angle of the Cherenkov light, about 42 degrees.

In februari 1987 a special event occurred. A supernova went off in the Large Magellanic Cloud. This was the closest supernova since the 1064 supernova that actually occurred in our own galaxy. The neutrino rate in the detectors increased by many orders of magnitude and within a range of 10 seconds 24 events were detected in Kamiokande, IMP and an iron wire chamber neutrino detector BAKSAN. The result is shown in Figure 6-3.

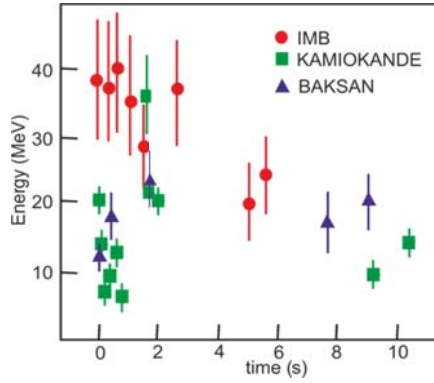


Figure 6-3: Arrival time and energy of the neutrinos from SN1987a

The detection of neutrinos from SN1987a changed the physics goal of the experiments from dominated by proton decay to dominated by neutrino physics. The IMB detector unfortunately sprang a leak and as it was placed in a salt mine destroyed its cavity and underground laboratory leaving the way free for Kamiokande to continue the work on neutrino physics.

The Advantage of the water detectors over the inverse beta decay experiments is that each event is individually measured and the direction from which the neutrino came that produced the interaction could be established. Kamiokande produced two major results namely a measurement of the electron-neutrino flux from the Sun and the atmospheric muon-neutrino flux as a function of the zenith angle. The former result is shown in Figure 6-4.

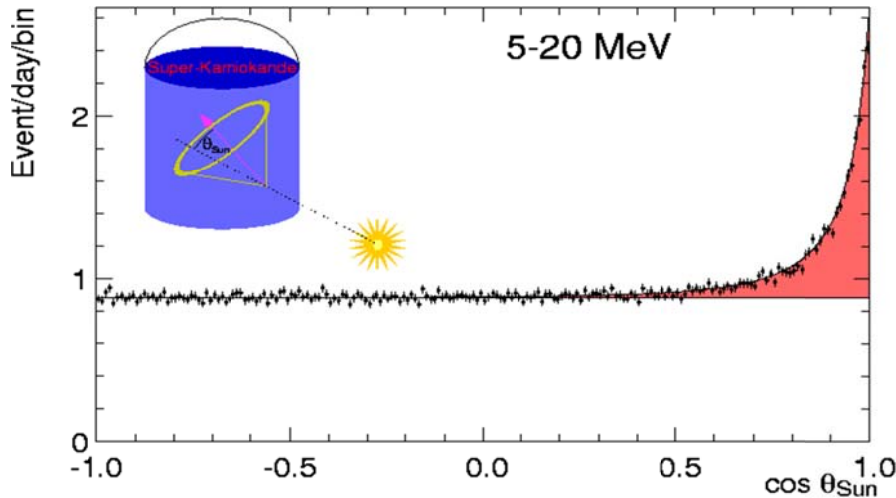


Figure 6-4: The intensity of the neutrinos measured in the Kamiokande experiment as a function of the angle with respect to the direction of the sun.

The distribution shows a clear excess of neutrinos coming from the sun on a background of atmospheric neutrinos. By integrating the solar peak and subtracting the constant background an estimate could be made of the flux coming from the Sun. As the energy threshold is set at 5 MeV this experiment is only sensitive to the neutrinos from the  $^8\text{B}$  decay in the Sun. The flux measured by the experiment is

$$\phi = (2.8 \pm 0.18 \pm 0.33) \times 10^6 \text{ [cm}^{-2}\text{s}^{-1}\text{]} \quad (6-13)$$

Compared to the predicted flux of

$$\varphi = (5.8 \pm 0.4) \times 10^6 [cm^{-2}s^{-1}] \quad (6-14)$$

So again a deficit of a factor of two compared to the model.

## 6.4 Oscillations

An explanation to explain the experimental deficit of neutrinos from the sun is that the neutrinos oscillate. In other words the the flavor of the neutrino is not constant as it travels but rather varies as a function of energy and distance from production. To see to this the assumption is made that the interaction eigenstates of the neutrino are not the same as the mass eigenstates. In other words a neutrino made in an interaction is built up of neutrino states of different mass. And neutrinos travelling through space are not a definite flavor.

We can write this mathematically by introducing three mass eigenstates neutrinos:  $\nu_1, \nu_2, \nu_3$  they are then related to the flavor eigenstates :  $\nu_e, \nu_\mu, \nu_\tau$  via a unitary transformation:

$$|\nu_f\rangle = \sum_m U_{fm} |\nu_m\rangle \quad (6-15)$$

Every mass eigenstates is of course the solution to the Dirac/Schrödinger/Klein-Gordon equation in free space and is therefore given by:

$$|\nu_m\rangle = e^{-ip_m \cdot r_m} = e^{-i(E_m t_m - p_m L)} \quad (6-16)$$

With  $p_m = \sqrt{E_m^2 - M_m^2} = E_m - \frac{M_m^2}{2E_m}$  and  $t = L/c$  we get for the mass eigenstates the equation

$$|\nu_m\rangle = e^{-i(\frac{M_m^2}{2E})L} \quad (6-17)$$

Assume now we have a flavor eigenstate  $|\nu_f\rangle$  produced as a mixture of mass eigenstates at time  $t=0$  then after a time  $t$  or distance  $L$  the flavor eigenstates will have evolved from

$$|\nu_f\rangle = \sum_m U_{fm} |\nu_m\rangle \quad (6-18)$$

To

$$|\nu_f\rangle = \sum_m U_{fm} e^{-i(\frac{M_m^2}{2E})L} |\nu_m\rangle \quad (6-19)$$

Of course at this point we can decompose each mass eigenstates into a set of flavor eigenstates and so we get:

$$|\nu_f\rangle = \left[ \sum_m U_{fm} e^{-i(\frac{M_m^2}{2E})L} U_{f'm}^* \right] |\nu_{f'}\rangle \quad (6-20)$$

So, in general, a state that starts off as a flavor eigenstates will, after a certain distance, evolve into a superposition of all flavor eigenstates. This of course allows for the disappearance of neutrinos of a certain flavor, while the other flavors remain undetected

through energy conservation. The probability of measuring flavor  $f'$  after a distance  $L$  if one starts with flavor  $f$  is given by

$$P(f \rightarrow f'; L) = |\langle \nu_{f'} | \nu_f(L) \rangle|^2 = \left| \sum_m U_{f'm} e^{-i(\frac{M_m^2}{2E})L} U_{fm}^* \right|^2 \quad (6-21)$$

Restricting ourselves to two flavors the unitary matrix can be written as

$$U = \begin{pmatrix} U_{e1} & U_{e2} \\ U_{\mu 1} & U_{\mu 2} \end{pmatrix} = \begin{pmatrix} \cos\vartheta & \sin\vartheta \\ -\sin\vartheta & \cos\vartheta \end{pmatrix} \quad (6-22)$$

Where the angle  $\vartheta$  parameterizes the initial mixing of the flavor eigenstates into the mass eigenstates. Insertion of (6-22) into (6-21) yields the following result:

$$P(f \rightarrow f'; L) = \sin^2 2\vartheta \sin^2 \left( \frac{1.27 \Delta M_{12}^2 [\text{eV}^2] L [\text{km}]}{E [\text{GeV}]} \right) \quad (6-23)$$

This therefore gives a natural explanation for the deficit in the solar neutrino flux. If the difference of the masses squared are such that the term in the bracket is a large number the spread of the energy of the neutrinos will cause only 50% of the initial electron neutrinos to be measured as electron neutrinos. The others will manifest themselves as muon or tau neutrinos and therefore be difficult to detect. Except in elastic neutral current scattering the interaction will be excluded by energy conservation as muons or taus must be made in the final state to conserve lepton flavor.

## 6.5 The SNO experiment

In order to prove the assumption that oscillations are causing the neutrino deficit from the Sun an experiment must be devised that is sensitive to all flavours of neutrinos. The Sudbury Neutrino Observatory constructed a water Cherenkov experiment but replacing conventional water by heavy water. The replacement of hydrogen by deuterium has the advantage that two additional interactions can take place. In addition to the conventional charged and neutral current scattering off electrons:



Also the deuteron disintegrations take place.



If the reactions (6-25) and (6-26) can be separated experimentally then the strengths of the NC scattering can be determined and therefore the rate of interactions caused by the sum of all flavour neutrinos. The experimental separation requires the detection of the neutron produced in the reaction (6-26). This is done in the experiment through the reaction



The detection of the delayed electron from the tritium decay gives determines the rate of the interaction (6-26) and therefore the intensity of the total neutrino flux from the sun.

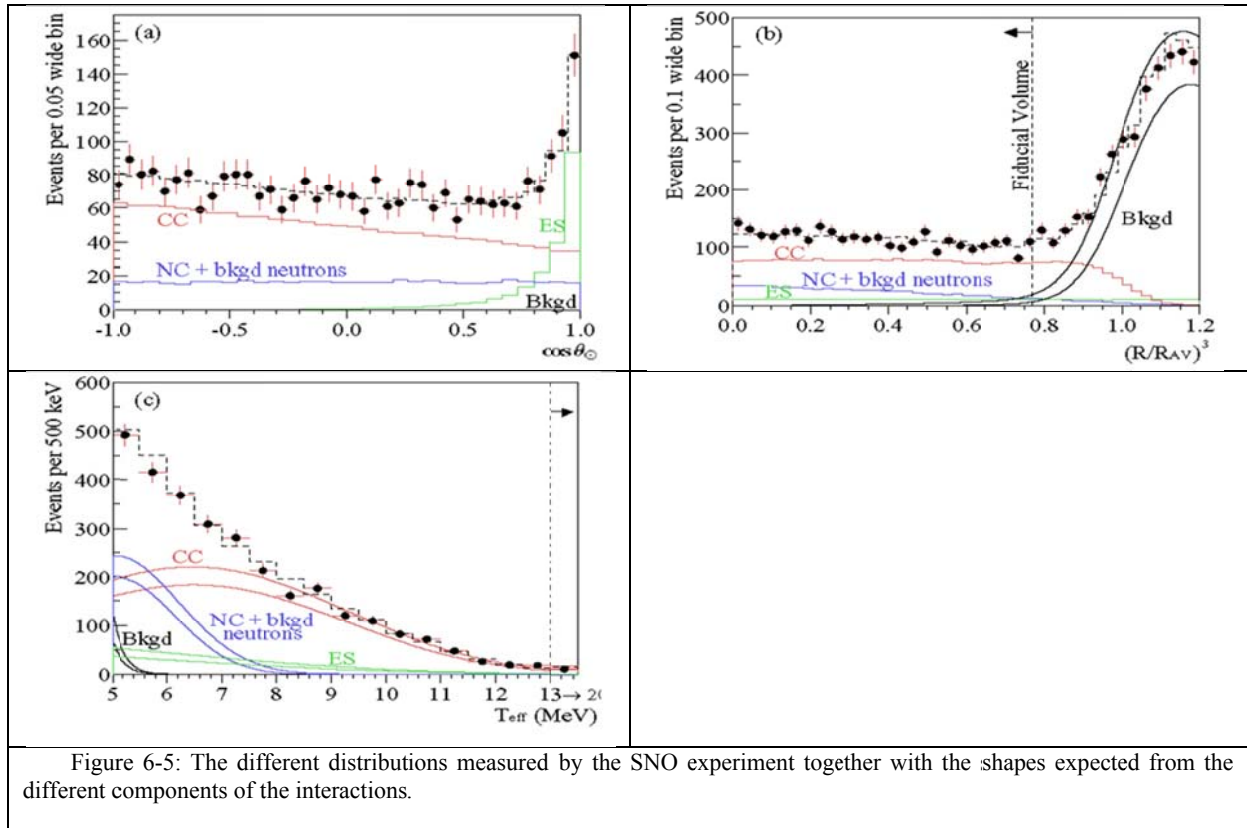


Figure 6-5: The different distributions measured by the SNO experiment together with the shapes expected from the different components of the interactions.

From the fit to the distributions in Figure 6-5 the intensity of the different neutrino interactions could be determined to be:

$$\varphi_{CC} = (1.76 \pm 0.06 \pm 0.09)10^6 [\text{cm}^{-2}\text{s}^{-1}] \quad (6-28)$$

$$\varphi_{ES} = (2.39 \pm 0.24 \pm 0.12)10^6 [\text{cm}^{-2}\text{s}^{-1}] \quad (6-29)$$

$$\varphi_{NC} = (5.09 \pm 0.44 \pm 0.45)10^6 [\text{cm}^{-2}\text{s}^{-1}] \quad (6-30)$$

From which the result for the different flavours was found to be

$$\varphi_e = (1.76 \pm 0.06 \pm 0.09)10^6 [\text{cm}^{-2}\text{s}^{-1}] \quad (6-31)$$

$$\varphi_{\mu\tau} = (3.41 \pm 0.45 \pm 0.47)10^6 [\text{cm}^{-2}\text{s}^{-1}] \quad (6-32)$$

Which is shown graphically in

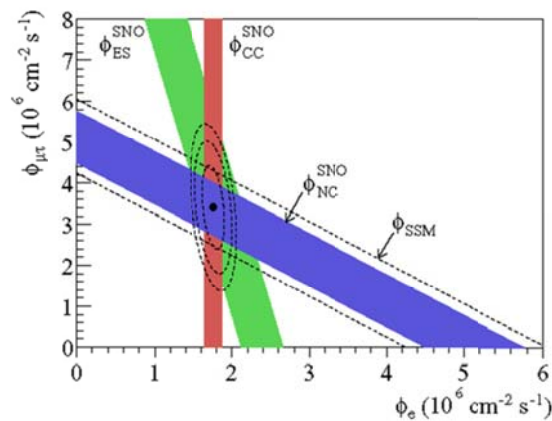


Figure 6-6: The determination of the ES, NC and CC rates in the SNO experiment. Each channel gives a band in the electron neutrino to other neutrino diagram. At the overlap approximately one third of all neutrinos are electron neutrinos.

The final result is therefore that the total flux of neutrinos from the sun are in excellent agreement with the solar model but that only about one third of all neutrinos coming from the sun are electron neutrinos when they arrive on earth.

## 6.6 Atmospheric Neutrinos

In addition to measuring the neutrinos from the sun the Kamiokande experiment also measured electron and muon neutrinos produced in cosmic ray interactions in the atmosphere. For the muon neutrinos again a deficit was observed. The deficit showed a dependence on the azimuthal angle of neutrino arrival direction (Figure 6-7). This angle is correlated with the distance from neutrino production to detection and so again indicates the presence of neutrino oscillations.

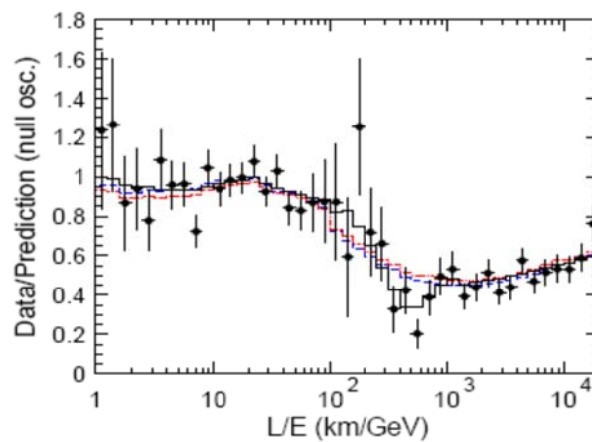


Figure 6-7: The ratio of muon neutrino rate measured to predicted assuming no oscillation as a function of the distance, determined from the azimuthal angle, divided by the measured energy. At values of  $L/E$  of about 100 km the measured intensity falls below the expectation for no oscillations. The coloured curves show the expectation in the presence of oscillations.

Whereas the muon neutrinos showed this clear oscillation the electron neutrinos showed no increase in the same region. The solar neutrino oscillations indicate a difference in neutrino masses squared of around  $10^{-5} \text{ eV}^2$ , whereas the atmospheric neutrinos indicate a difference in masses squared of about  $3 \times 10^{-3} \text{ eV}^2$ .

## 6.7 The Wolfenstein-Mikheev-Smirnow effect

If a neutrino state travels through matter it will undergo coherent forward scattering. Each interaction part of the mass eigenstates will behave differently and therefore the oscillation pattern will be modified. The forward scattering amplitude ( $f$ ) is related to the total cross section via the optical theorem

$$\sigma_{tot} = \frac{4\pi}{k^2} \text{Im}(f(0)) \quad (6-33)$$

The total cross section for electron neutrinos is significantly higher than for muon and tau neutrinos as only the NC process is possible for these neutrino types. The electron neutrino part of the wave function of any mass eigenstates will therefore pick up a phase shift with respect to the remainder of the wave function. The interactions can be added as a potential term in the equation of motion.

$$V_{\nu_e} = \sqrt{2}G_F N_e \quad (6-34)$$

Where  $N_e$  is the electron density in matter and  $G_F$  is the Fermi coupling constant. We can now discuss the system as a two component oscillation as we are only interested in the difference between the electron neutrino and the others. We can write this as two coupled equations of motion. We start with the initial mixing of the neutrinos.

$$\begin{pmatrix} \nu_e \\ \nu_a \end{pmatrix} = \begin{pmatrix} \cos \vartheta & \sin \vartheta \\ -\sin \vartheta & \cos \vartheta \end{pmatrix} \begin{pmatrix} \nu_1 \\ \nu_2 \end{pmatrix} \quad (6-35)$$

The evolution of the flavor content of the wave function can then be written as

$$i \frac{d}{dx} \begin{pmatrix} \nu_e \\ \nu_a \end{pmatrix} = \frac{1}{2E} M^2 \begin{pmatrix} \nu_e \\ \nu_a \end{pmatrix} \quad (6-36)$$

$$M^2 = \left[ \begin{pmatrix} \cos \vartheta & \sin \vartheta \\ -\sin \vartheta & \cos \vartheta \end{pmatrix} \begin{pmatrix} -\Delta m^2 & 0 \\ 0 & \Delta m^2 \end{pmatrix} \begin{pmatrix} \cos \vartheta & -\sin \vartheta \\ \sin \vartheta & \cos \vartheta \end{pmatrix} + 2E \begin{pmatrix} \sqrt{2}G_F N_e & 0 \\ 0 & -\sqrt{2}G_F N_e \end{pmatrix} \right]$$

So the matter eigenstates are not purely given by the mass difference but also by the difference in potential energy. We can now define the new mass eigenstates in matter as

$$\begin{pmatrix} \nu_{1m} \\ \nu_{2m} \end{pmatrix} = \begin{pmatrix} \cos \vartheta_m & -\sin \vartheta_m \\ \sin \vartheta_m & \cos \vartheta_m \end{pmatrix} \begin{pmatrix} \nu_e \\ \nu_a \end{pmatrix} \quad (6-37)$$

Where  $\vartheta_m$  can be extracted by solving the eigenvalue problem

$$\begin{pmatrix} \cos \vartheta_m & -\sin \vartheta_m \\ \sin \vartheta_m & \cos \vartheta_m \end{pmatrix} M^2 \begin{pmatrix} \cos \vartheta & \sin \vartheta \\ -\sin \vartheta & \cos \vartheta \end{pmatrix} = \frac{1}{2} \begin{pmatrix} -\Delta_m & 0 \\ 0 & \Delta_m \end{pmatrix} \quad (6-38)$$

Which gives mass differences

$$\Delta_m = \Delta m^2 \sqrt{(a - \cos 2\vartheta)^2 + \sin^2 2\vartheta} \quad (6-39)$$

$$a = \frac{2\sqrt{2}E G_F N_e}{\Delta m^2}$$

And newly defined mixing angles

$$\sin^2 2\vartheta_m = \frac{\sin^2 2\vartheta}{(a - \cos 2\vartheta)^2 + \sin^2 2\vartheta} \quad (6-40)$$

This gives the possibility that the finally observed mixing is significantly larger than it would be in vacuum, depending on the electron density. Figure 6-8 shows the behaviour of the mixing parameter as a function of the parameter  $a$ . For specific electron density and neutrino energy the mixing will be significantly enhanced to maximum mixing.

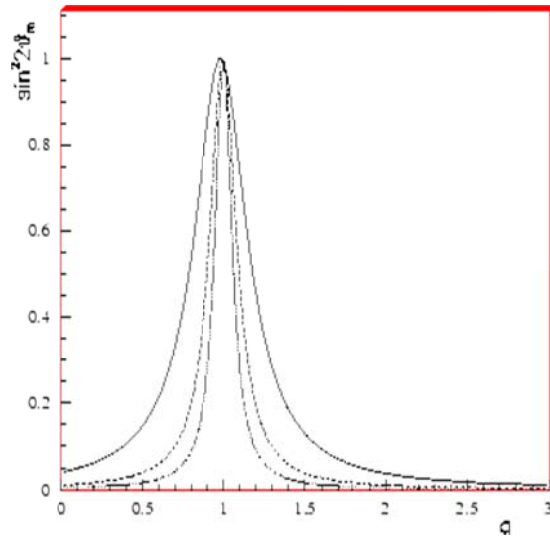


Figure 6-8: the behaviour of the mixing angle as a function of  $a$  for different values of the vacuum mixing angle. From inside out the values are  $\sin^2 2\theta = 4 \times 10^{-3}, 10^{-2}, 4 \times 10^{-2}$  respectively.